Bulletin of the Seismological Society of America, Vol. 101, No. 5, pp. 1979–2000, October 2011, doi: 10.1785/0120100200

Observations and Modeling of Strong Ground Motions for the 9 October 1995 M_w 8 Colima–Jalisco, Mexico, Earthquake

by M. Chavez, K. B. Olsen, E. Cabrera, and N. Perea

Abstract The Colima–Jalisco (CJ) region in northwestern Mexico has generated large-magnitude earthquakes at least since 1800. For example, during the last century, three large, destructive, shallow-thrust subduction earthquakes occurred on 3 and 18 June 1932 with M_S of 8.2 and 8, respectively, and on 9 October 1995 (M_w 8, M_S 7.4). This historical seismicity and the lack of seismic recordings in the CJ region pose important constraints for the computation of reliable seismic-hazard studies for sites in this region of Mexico. Towards this aim, we have used a hybrid method to generate broadband (BB) synthetics for the M_w 8 CJ 1995 earthquake for the recording sites of the near (MZ) intermediate (CG), and far (COL) fields. The low-frequency (LF, $\leq$0.5 Hz) synthetics were simulated by applying a 3D finite-difference method, and the high frequencies (HF, $>$0.5 Hz) were generated by the empirical Green's function technique. Finally, matched filters were applied to the LF and HF synthetics to obtain the BB time series. The LF synthetics were computed from a finite-fault description of the source with four asperities in a 2.5D model constrained by gravity and seismological data. Our preferred model includes an approximation of a thin accretionary prism. For the HF modeling, we also used the four-asperity source model as well as the recordings of the foreshock and aftershock of the M_w 8 1995 mainshock. Based on the comparisons of the BB synthetics with the observed strong ground motions for the 1995 CJ earthquake at the three stations, we believe that our hybrid method is a first step toward the generation of more reliable estimates of the seismic hazards in CJ region. Further improvement in the hazard estimates depends on the urgent deployment of seismological and strong ground motion infrastructure in the CJ region.

Online Material: Supplementary figures of the empirical Green's functions, low-frequency, high-frequency, and broadband synthetics and their fit to data.

Introduction

The high seismic potential of the Colima–Jalisco (CJ) region in Mexico has been demonstrated over the last several centuries. For example, in the period from about 1800 to 1900, large earthquakes occurred in the region on the following dates (see Nishenko and Singh, 1987): 25 March 1806 (M_S 7.5), 31 May 1818 (M_S 7.7), and 20 January and 16 May 1900 (M_S 7.6 and 7.1, respectively). More recently, other large shallow-thrust subduction earthquakes occurred on 3 and 18 June 1932, with M_S of 8.2 and 8, respectively, on 30 January 1973 (M_w 7.6, M_S 7.3), on 9 October 1995 (M_w 8, M_S 7.4), and on 22 January 2003 (M_w 7.4, M_S 7.3; see Fig. 1). The historical seismic information available for the CJ region suggests that the recurrence time for M ~8 earthquakes (such as the M_S 8.2 1932 event) ranges from 77 to 126 yr (Nishenko and Singh, 1987).

For the 1995 earthquake and for its largest (6 October 1995 M_w 5.75) foreshock and (12 October 1995 M_w 5.92) aftershock (Fig. 2), good quality, free-field, accelerographic records were obtained at stations Manzanillo (MZ), Ciudad Guzman (CG), and Guadalajara (COL) with epicentral distances to the mainshock in the near field (50 km), intermediate field (140 km), and far field (240 km), respectively (see Fig. 3). However, besides these records, few accelerographic recordings are available in the CJ region for large (or small) magnitude events. Thus, in order to obtain better estimates of the seismic hazard for this densely populated and very active socioeconomical region of Mexico, there is a need to generate synthetic accelerograms associated with plausible damaging seismic scenarios. Towards this objective, we apply a hybrid technique to generate broadband (BB) synthetic

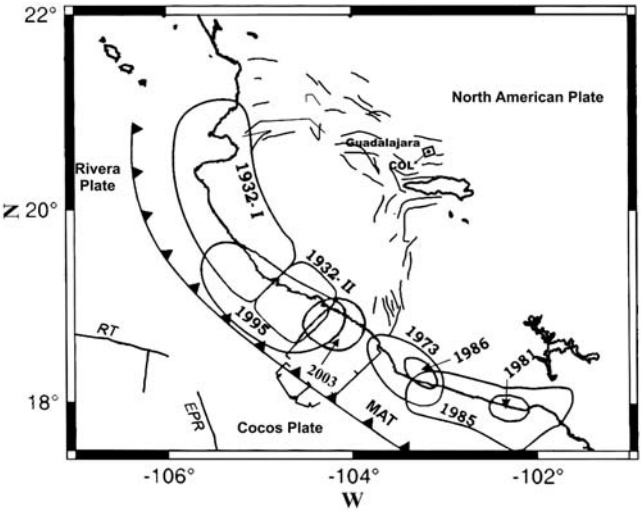

Figure 1. Rupture areas for the 3 (1932-I) and 18 (1932-II) June 1932, 31 January 1973, 9 October 1995, 22 January 2003, and 19 September 1985 earthquakes (modified from Pacheco and Kostoglodov, 1999).

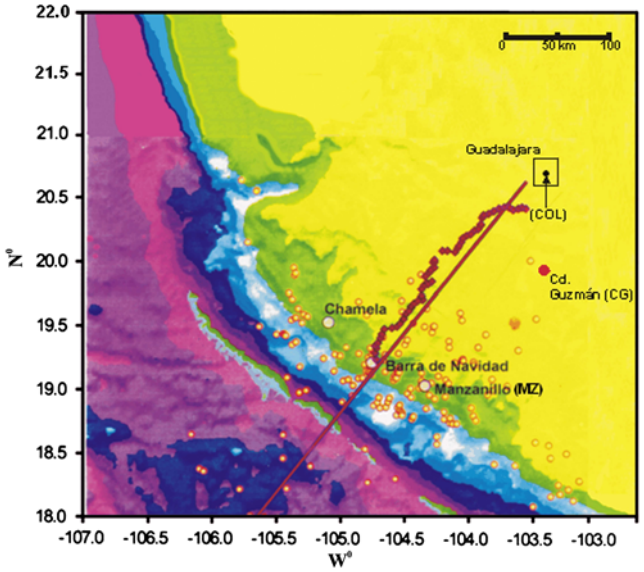

Figure 3. Survey line for gravity (continuous line), gravimetric stations (diamonds), and seismic data (small circles) used by Bandy *et al.* (1999). Location of the accelerographic stations Manzanillo (MZ), Ciudad Guzman (CG) and COL in Guadalajara (modified from Bandy *et al.*, 1999). The color version of this figure is available only in the electronic edition.

accelerograms at MZ, CG, and COL for the 9 October 1995, M_w 8 CJ earthquake.

The paper is divided into the following sections: a discussion of the main features of the seismotectonics of the CJ region and of the 1995 earthquake, an analysis of the horizontal accelerographic recordings obtained for the mainshock and the largest foreshock and aftershock of the 1995 event, a description of the applied hybrid BB modeling technique, the results obtained for the BB modeling of the strong ground motions at MZ, CG and COL for the 1995 earthquake, and the conclusions.

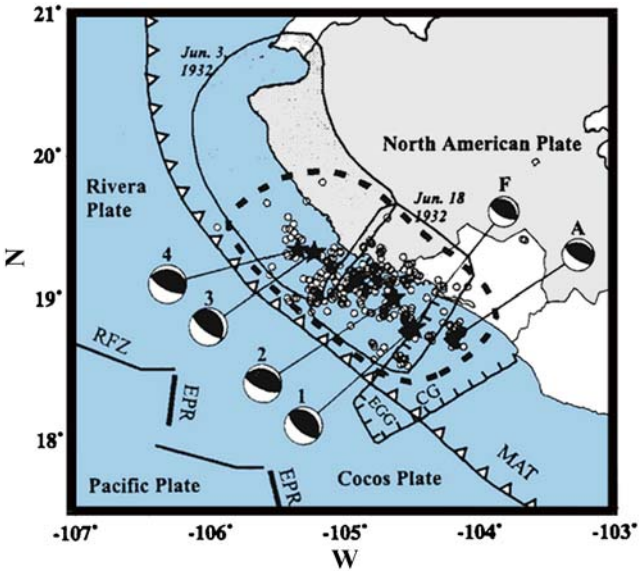

Figure 2. Rupture areas for 3 and 18 June 1932 earthquakes, epicentral locations and focal mechanisms for the 9 October 1995 mainshock 1, the foreshock F (6 October), the largest aftershock A (12 October), the outline of the aftershock zone (dashed), and the 4 subevents (1–4) interpreted by Escobedo *et al.* (1998) as the source for the main event. RFZ, Rivera fracture zone; EPR, East Pacific rise; EGG, El Gordo graben; CG, Colima graben; MAT, Middle American trench (modified from Escobedo *et al.*, 1998). The color version of this figure is available only in the electronic edition.

Seismotectonics of the Colima–Jalisco Region and the 9 October 1995 M_w 8 Earthquake

The seismotectonics of the CJ region are mainly associated with the subduction of the Rivera plate beneath the North American plate (NOAM) in the Jalisco–Colima zone in the northern part of the Middle American Trench in western Mexico. The main tectonic features of the region of interest were synthesized by Escobedo *et al.* (1998) and are shown in Figure 2. Note that the rupture area (about 160 km in length by 90 km in width) of the 9 October 1995 earthquake included approximately 40% and 100% of the rupture areas of the 3 and 18 June 1932 earthquakes, respectively. Also, Escobedo *et al.* (1998) proposed that the 1995 mainshock was made up of four subevents (S1–S4, see Fig. 2). The seismic moments (M_0), the moment magnitudes (M_w), and the seismic source parameters of the mainshock and its four subevents as well as of the largest foreshock and aftershock are listed in Table 1. From Figure 2 and Table 1, it can be concluded that the source mechanisms of the foreshock and aftershock are similar to the average mechanism of the 1995 mainshock; in other words, the three events are shallow-dipping, thrust-fault earthquakes in agreement with the relative plate motions for the Rivera-NOAM and the Cocos-NOAM plate boundaries.

Table 1
Source Parameters of the Mainshock, Largest Foreshock and Aftershock, and Four Subevents of the 9 October 1995 M_w 8 Earthquake*

Event	Depth (km)	Strike (°)	Dip (°)	Rake (°)	M_0 (N·m)	M_w
Foreshock	18	314	29	104	4.28×10^{17}	5.75
Mainshock	24	306	26	94	1.84×10^{20}	8.00
Aftershock	21	290	25	76	7.75×10^{17}	5.92
Subevent 1	28	320	28	98	4.39×10^{19}	7.06†
Subevent 2	31	286	25	84	4.92×10^{19}	7.09†
Subevent 3	19	338	25	119	4.13×10^{19}	7.04†
Subevent 4	20	282	26	75	5.00×10^{19}	7.10†

*Modified from Escobedo *et al.* (1998).
†Estimated from the M_0 values by using $M_w = (\log M_0/1.5) - 10.7$ (Kanamori and Anderson, 1975).

The age of the Rivera plate varies between 10 and 15 m.y. (Klitgord and Mammerickx, 1982; Kostoglodov and Bandy, 1995), and its rate of subduction below the NOAM is estimated to be between 2 and 5 cm/yr (Kostoglodov and Bandy, 1995). Regardless of this slow convergence rate, the periods of interseismic activity between large earthquakes in this region appear to be shorter than in the Cascadian subduction zone (Pacific Northwest region). For example, between 1932 and 2003, the subduction process of the Rivera-NOAM plates has generated the three large and destructive earthquakes mentioned in the Introduction (3 and 18 June 1932 and 9 October 1995, see Figs. 1 and 2). In comparison, the Cascadian subduction zone has an average recurrence period for megathrust events of about 500 yr (e.g., Heaton and Hartzell, 1986).

Based on data obtained from gravity measurements constrained by seismicity data (see Fig. 3), Bandy *et al.* (1999) proposed a model for the geological structure of the subducting and continental plates in the CJ region (see Fig. 4). Among other findings, they proposed that the thickness of the continental crust averages 38 km and thickens, gradually, towards the continent up to 44 km. They also concluded that the density of the upper part of the subducting plate increases at a depth of 30 km, probably reflecting a phase transition of basalt to eclogite. Figure 4 suggests that the subducting slab initially dips at an angle that varies from 9° to 16° down to a depth of about 20 km, and then the dip angle of the slab gradually increases to about 50° at depths below 50 km. In the model, the continental crust is made of an upper layer with a density of 2800 kg/m^3, a lower crustal layer with a density of 2900 kg/m^3, and a thin sedimentary layer with a density of 2300 kg/m^3 in the continental slope zone. Bandy *et al.* (1999) modeled the Rivera plate as consisting of three layers with densities of 2500, 2900, and 3320 kg/m^3, and the upper mantle beneath it with a density of 3300 kg/m^3, as under the continental crust.

Analysis of the Recordings of the 9 October 1995 Mainshock, the Largest (6 October) Foreshock, and the Largest (12 October) Aftershock

Three-component strong ground motion records were obtained with the Jalisco Accelerographic Network (JAN) of free-field autonomous SSA-2 and downhole Kinemetrics accelerographs (Chavez, 1993, 1995), and a DCA-333R Terra Technology accelerograph operated by the Centro de Instrumentación y Registro Sísmico A.C. (CIRES) for the 9 October 1995 mainshock as well as for the 6 October 1995 foreshock and 12 October 1995 aftershock, hereafter referred

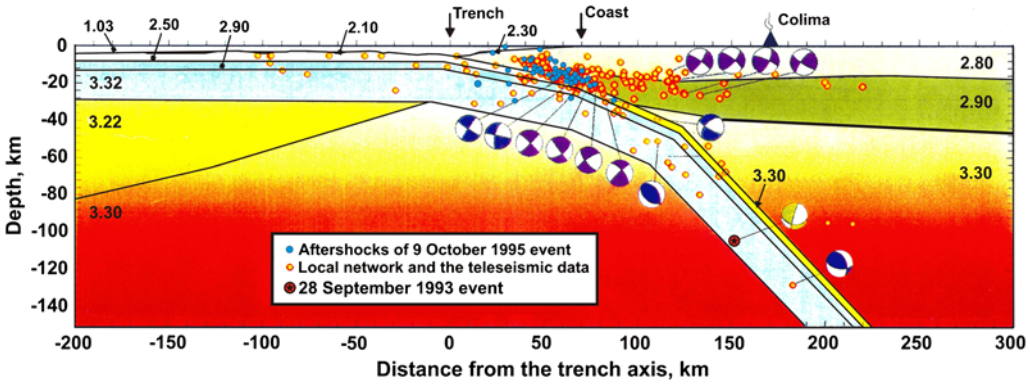

Figure 4. Recent seismicity, geometry, and density (g/cm^3) of the subducting and continental plates for a 500-km profile (for location, see Fig. 3) in the region of interest (modified from Bandy *et al.*, 1999). The color version of this figure is available only in the electronic edition.

to as events M, F, and A, at the accelerographic stations of Manzanillo (MZ, CIRES), Ciudad Guzman (CG, JAN) and Guadalajara's (JAN) COL surface and downhole (see Fig. 3). Incidentally, the JAN network, which had 11 free-field and two downhole stations at Guadalajara and one free-field station at CG (Chavez, 1993, 1995) and had a 100% recording success for the M_w 8 1995 CJ earthquake, stopped functioning in 1997 due to lack of interest and economical support of the local, state, and federal authorities.

The three free-field accelerographic stations of MZ, CG, and COL were located on top of soil layers, and COL's downhole station was set on a basaltic rock at 35 m depth (Chavez, 1993, 1995). In Figures 5–7, we show the west-east (WE) and north-south (NS) accelerograms and the associated Fourier

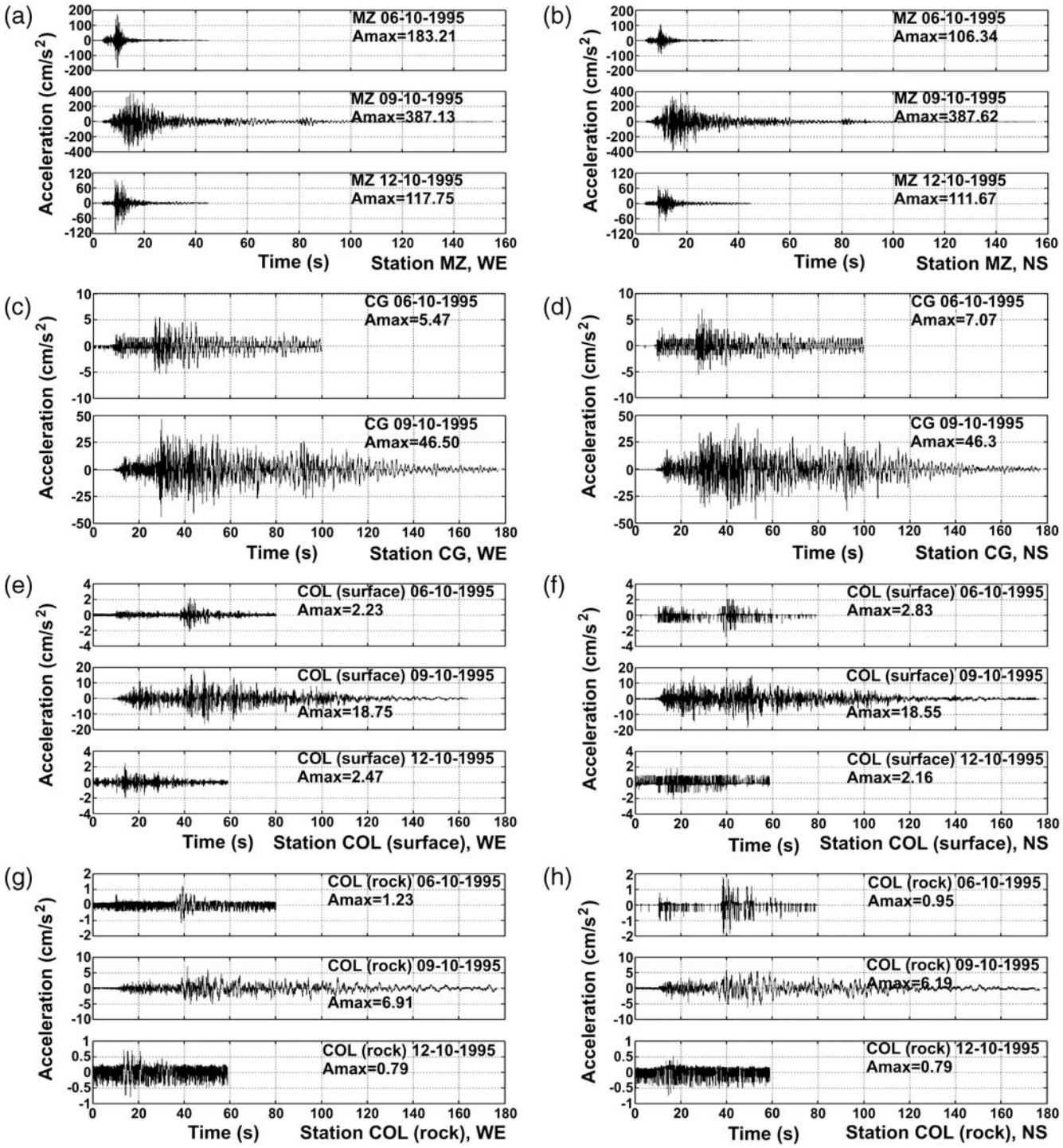

Figure 5. Accelerograms observed at stations (from top to bottom) (a,b) MZ, (c,d) CG, (e,f) $COL_{surface}$, and (g,h) COL_{rock}, for the 9 October 1995 earthquake mainshock and the largest foreshock and aftershock (missing at CG). Left, WE. Right, NS components.

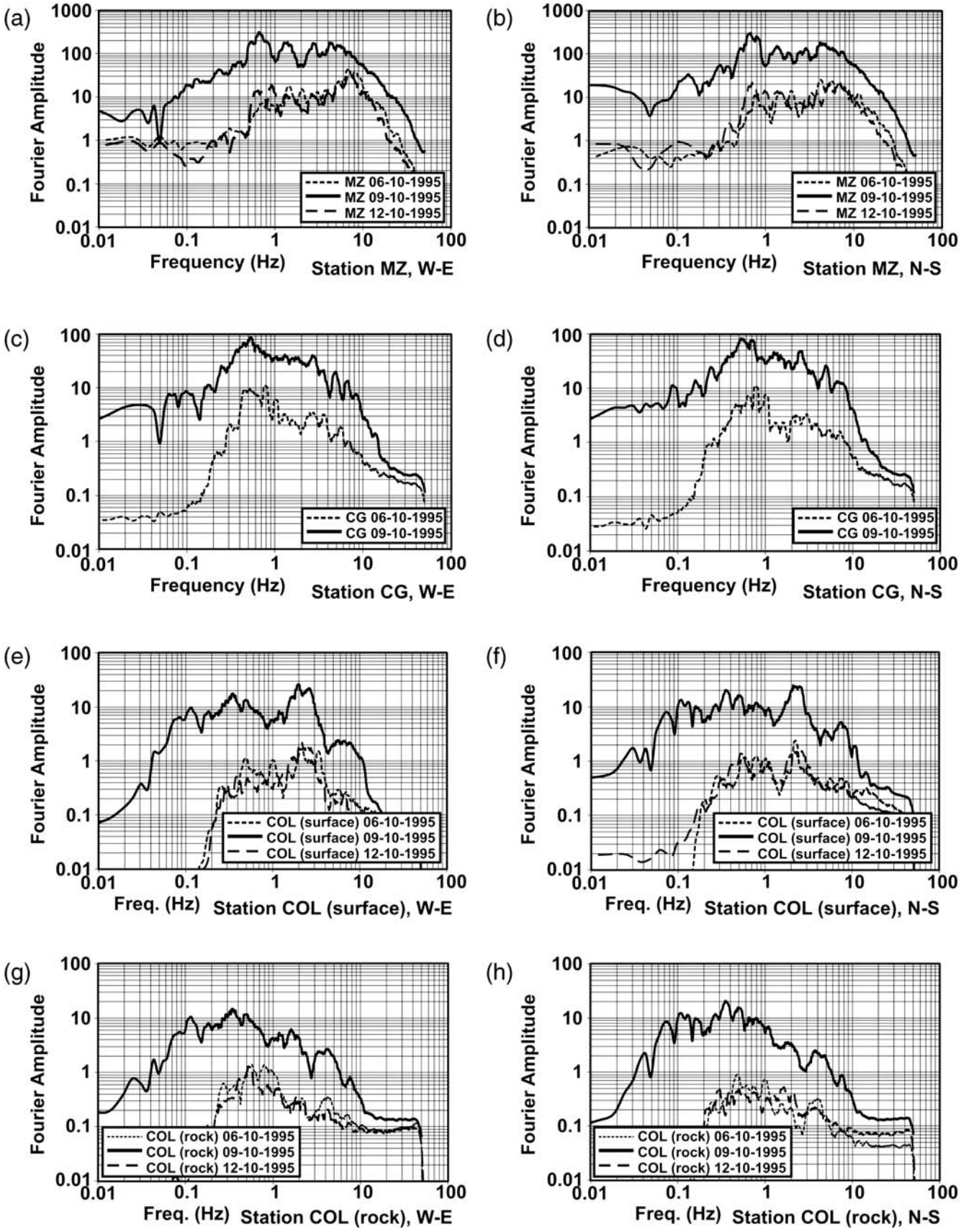

Figure 6. Fourier amplitude spectra of the accelerograms shown in Figure 5 for stations (from top to bottom) (a,b) MZ, (c,d) CG, (e,f) $COL_{surface}$, and (g,h) COL_{rock}. Left, WE component. Right, NS component.

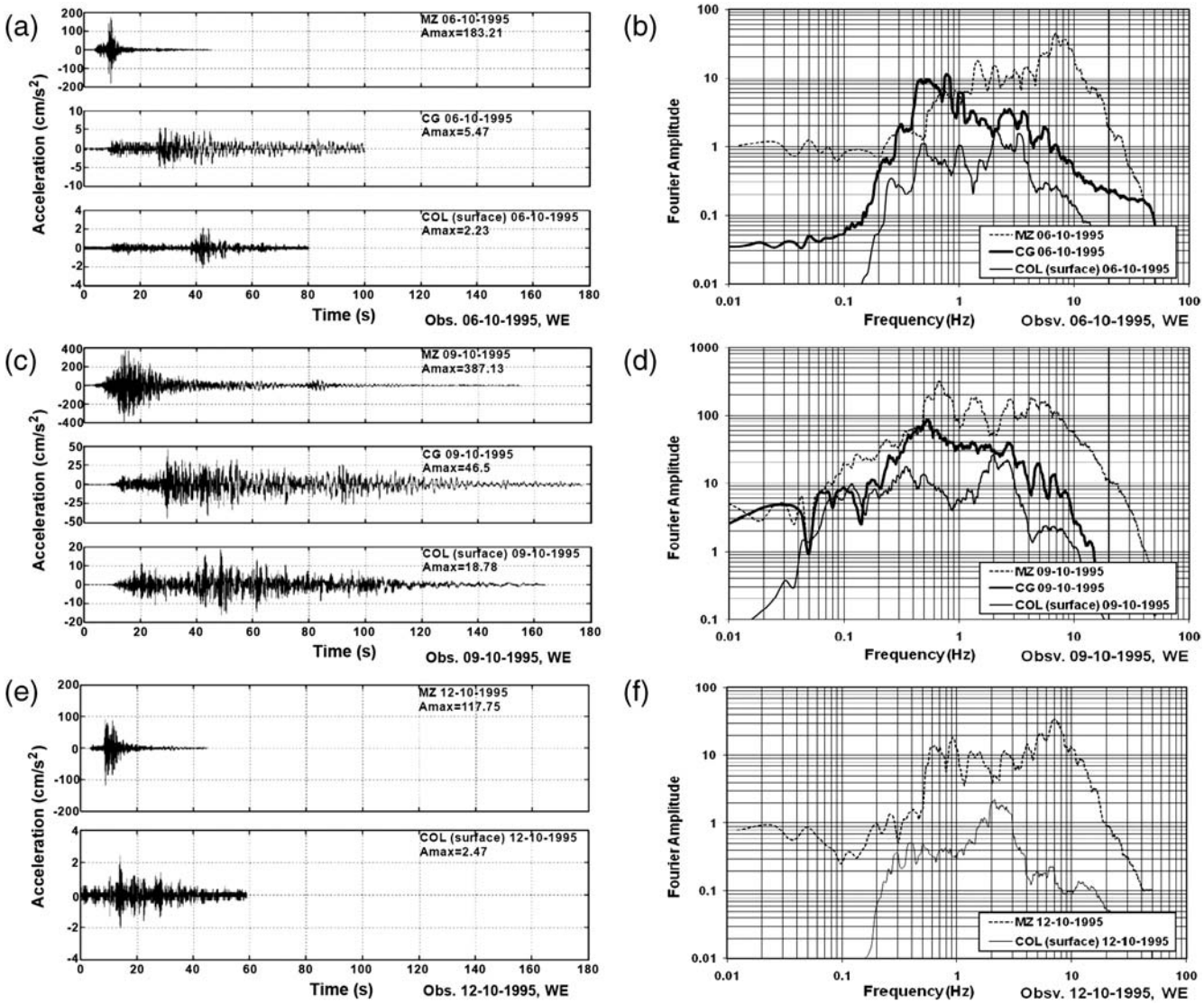

Figure 7. (a,c,e) Accelerograms for the WE component at stations MZ, CG, and $COL_{surface}$ for the 6, 9, and 12 October 1995 largest foreshock, mainshock, and aftershock (missing for CG). (b,d,f) Fourier amplitude spectra of the accelerograms shown in (a,c,e), respectively.

amplitude spectra (the vertical components are presented in Chavez, 2000) obtained at stations MZ, CG and COL for events F, M, and A. In Figures 5 and 6, we present the time- and frequency-domain information for the WE and NS recordings of the events at each of the stations, and in Figure 7 is shown a comparison of the WE components recorded at MZ, CG, and COL stations for the F, M, and A events.

From the observations at the near-field station MZ shown in Figure 5a,b, the horizontal peak ground accelerations (PGA) were ~400 cm/s^2 for the M event, ~200 cm/s^2 for the F event, and ~100 cm/s^2 for the A event. The duration of the acceleration time series for event M was ~160 s but ~45 s for F and A. The frequency-domain characteristics of the MZ records on the horizontal components are shown in Figure 6a,b. The maximum values of the Fourier amplitudes for the M event are about one order of magnitude higher (i.e., ~300 cm/s) than for the F and A events (i.e., ~30 cm/s). Those maxima occur at 0.7, 1.5, 3, and 4 Hz, with spectral decay starting at about 5 Hz for M and 7 Hz for F and A.

In Figure 5c,d, we show the recordings for the M and F events (the records for the A event were partially damaged) at CG intermediate-field station (see Fig. 3). From these plots, it can be seen that the peak ground acceleration (PGA) for the WE and NS directions was ~46 cm/s^2 for the M event and that the corresponding values of PGA for the WE and NS components for the F event were ~7 cm/s^2 and 5.5 cm/s^2, respectively. The duration of the time series was ~180 s for M and ~100 s for F. The frequency-domain characteristics of the CG records in the WE and NS directions are shown in Figure 6c,d, respectively. As in the case of the MZ recordings, the maximum values of the Fourier amplitudes at CG

for the M event are about one order of magnitude higher (i.e., maximum amplitudes of ~100 cm/s) than for the F event (i.e., maximum values of ~10 cm/s). Those maxima occur at 0.5 and 2.5, 5, 6, and 7 Hz, and the drop-off of the spectral values starts at ~3 Hz for M and 4–5 Hz for F.

In Figure. 5e,f, we show the recordings for the M, F, and A events at the COL surface far-field station (see Fig. 3). From those figures, we notice that the PGA along the WE and NS directions for the M event were ~19 cm/s^2, and that the corresponding values of PGA along the WE and NS components for the F and A events varied from ~2 to 3 cm/s^2. The duration of the time series was ~160 s for M, 80 s for F, and ~60 s for A. The frequency-domain characteristics of the COL surface records in the WE and NS directions are shown in Figure 6e,f, respectively. The maxima occur at about 0.1, 0.35, and 2–3 Hz for the M event and at ~0.4–0.5 Hz and 2–3 Hz for the F and A events, respectively, and the drop-off of the spectral values starts at ~3 Hz for the three events.

In Figure 5g,h, we show the recordings for the M, F, and A events at COL rock, the downhole far-field station (see Fig. 3). The PGA on the WE and NS components for the M event were ~7 and 6 cm/s^2, respectively, and ~1 cm/s^2 for the F and A earthquakes. The duration of the time series was ~170 s for event M, 80 s for the F event, and ~60 s for the A event. The frequency characteristics of the COL rock records on the WE and NS components are shown in Figure 6g,h, respectively. From those figures, it can be concluded that the energy distribution with frequency corresponding to the recordings of the events M, F, and A are similar in shape up to 10 Hz, except for frequencies of less than 0.2 Hz; also, as in the case of the MZ and CG recordings, the maximum values of the Fourier amplitudes at COL rock station for the M event are about one order of magnitude higher (i.e., maximum amplitudes of ~15 cm/s) than for the F and A events (i.e., maximum values of ~1.0 cm/s). Those maxima occur at ~0.1 and 0.3 Hz for the M event and at ~0.5, 1, 2, and 4 Hz for the F and A events; the drop-off of the spectral values starts at ~7 Hz for the M, F, and A events.

In Figure 7a,c,e, we show a comparison of the WE components recorded at the MZ, CG, and COL surface stations for the F, M, and A events, respectively. Notice that in this figure, the attenuations with distance from the epicenter of the recorded signals, in other words, the PGA for the F, M, and A events, are ~200, 400, and 120 cm/s^2 at MZ (epicentral distance of ~50 km), compared to ~6 and 46 cm/s^2 at CG (epicentral distance of ~140 km), and 2, 19, and 2.5 cm/s^2 at COL (epicentral distance of ~240 km), respectively. Also notice in Figure 7b,d,f the large-amplitude high-frequency content from about 1 to 10 Hz of the MZ signal, compared to that at the CG and COL surface, which occurs from ~0.3 to 3 Hz.

From the observations discussed in the previous paragraphs, we can conclude that (1) the time and frequency content characteristics of the recorded M, F, and A events of the CJ 1995 M_w 8 earthquake, recorded at the surface of each of the stations MZ, CG, COL, and COL rock are very similar (except, as expected, for frequencies < 0.2 Hz), and (2) their differences in amplitudes are associated with the differences in their respective magnitudes (M_w 8 for M versus M_w 5.75 and 5.92 for F and A, respectively) as well as the attenuation with distance of the seismic energy propagating in the CJ region. In other words, except for a magnitude-related scale factor, the source, path, and respective local effects associated with the three events at each station are basically the same. We also notice that at several of the stations, there are trains of waves representing the large-amplitude ground motions for the M event, which are likely associated with the four subevent ruptures proposed by Escobedo *et al.* (1998). Finally, from the comparison of the Fourier amplitudes of the surface recording (Fig. 6e,f) versus the rock Fourier amplitudes (Fig. 6g, h), we can conclude that COL surface station shows important site effects between 1.5 and 3 Hz, as discussed by Chavez (1995, 2000).

Broadband Modeling Procedure

During the last 12 yr, a number of hybrid low-frequency/high-frequency (LF/HF) techniques to generate BB synthetic ground motions have been proposed by several authors, including Kamae *et al.* (1998), Hartzell *et al.* (1999), Graves and Pitarka (2004), and Liu *et al.* (2006). All of them use a deterministic 3D wave propagation method to generate LF synthetics and a theoretical (1D frequency-wave number; Liu *et al.*, 2006), stochastic (Hartzell *et al.*, 1999; Graves and Pitarka, 2004), or empirical Green's function (Irikura, 1998; Kamae *et al.*, 1998) method for simulating the HF ground motions. Then, summing the long-period and HF motions, after passing them through a pair of matched filters, allows the computation of the BB synthetics. Recently, the use of LF deterministic synthetics with local scattering operators to generate BB synthetics was proposed by M. Mai and K. B. Olsen (unpublished manuscript, 2010).

In the following, we present BB synthetics in the near, intermediate, and far fields for the 9 October 1995 M_w 8 CJ earthquake. Considering the similarities in the time-domain and frequency-domain characteristics of the strong ground motion observations of the main and the larger foreshock and aftershock of the earthquake discussed in the previous section, we followed the general format of the hybrid techniques proposed by Hartzell (1978) and Irikura (1986) for the HF modeling.

Low-Frequency Modeling

The long-period ($\leq$0.5 Hz) wave field was simulated using a staggered-grid finite-difference method to solve the 3D elastic equation of motion to a level of accuracy that is fourth order in space and second order in time, as implemented by Olsen (1994). The earthquake source is implemented in the finite-difference grid by adding $-M_{ij}/\mathrm{Vol}$ to τ_{ij}, where M_{ij} is the ij-th component of the moment tensor for the earthquake, Vol is the cell volume, and $\tau_{ij}(t)$ is the ij-th

component of the stress tensor on the fault at time t (Olsen *et al.*, 1995). The simulation used the absorbing boundary conditions by Cerjan *et al.* (1985) at the sides and bottom of the model and free-surface boundary condition FS2 by Gottschaemmer and Olsen (2001). Anelastic attenuation and surface topography were omitted in the finite difference (FD) simulations; however, the effects of these features are expected to be small or negligible for the long-period waves generated in our regional crustal model.

High-Frequency Modeling

The HF (>0.5 Hz) synthetics were generated with the empirical Green's function (EGF) method (Hartzell, 1978, Irikura, 1986), which uses the strong ground motions, associated with the rupture of a finite seismic source $U(t)$, which can be made up of several asperities (or subevents) of a large-magnitude earthquake by the superposition of the ground motions of small magnitude events, $u(t)$, produced by the ruptures of a finite number of elementary sources or subfaults located in the asperities or subevents of the large-magnitude event. As suggested by Irikura (1986, 1998) and Kamae *et al.* (1998), $U(t)$ can be obtained by applying equation (1):

$$U(t) = C \sum_{i=1}^{N} \sum_{j=1}^{N} \frac{r}{r_{ij}} F(t - t_{ij}) \cdot u(t), \tag{1}$$

where

$$t_{ij} = \frac{r_{ij} - r_0}{V_s} + \frac{\xi_{ij}}{V_r}, \tag{2}$$

and

$$F(t) = \delta(t) + \frac{1}{n'} \sum_{k=1}^{(N-1)n'} \delta\left[t - (k-1)\frac{\tau}{(N-1)n'}\right]. \tag{3}$$

Here, C is the stress-drop ratio of the large and the small events, N is the number of elementary sources, r and r_{ij} are the distances from the site to the hypocenter of the small event and to the ij-th subfault, respectively, $F(t)$ is a filtering function, r_0 is the distance from the site to the starting point of rupture on the fault plane of the large event, V_S is the shear-wave velocity of the propagation media, V_r is the rupture velocity, ξ_{ij} is the distance between the hypocenter and the ij-th elementary source, n' is a constant that prevents the generation of artificial periodicity in the synthetics, and τ is the rise time of the large event. The number of elementary sources, N, is computed by the scaling relation between the ratio of the seismic moment of the large (M_0) and the small (m_0) earthquakes:

$$M_0/m_0 = CN^3. \tag{4}$$

An important assumption of the EGF method is that the large and the small events follow the ω^2 model and have a constant stress drop; this implies that the source-displacement spectrum has a flat level at LFs and an omega-square decay at high frequencies beyond the corner frequency. We follow the suggestion of Frankel (1995) as well as Hartzell *et al.* (1999), expressing the elementary source area as the ratio of the seismic moments of the small and large events to the 2/3 power multiplied by the large-event rupture area.

Broadband Synthetics for the 9 October 1995 M_w 8 Colima–Jalisco Earthquake

Low-Frequency Synthetics

We simulated long-period (≥ 2 s) seismic waves generated by the 9 October 1995 M_w 8 earthquake using the 3D finite-difference scheme described in the previous section. The dimensions of the model were 354.6 km (length) by 163.8 km (width) by 163.2 km (depth) (see Figs. 8a and 9 and Table 2). We used a 2.5D model of the CJ subduction zone (see Fig. 9) based on the results obtained by Bandy *et al.* (1999) to represent the geologic structure and the densities of its layering (see Fig. 4) as well as the (slightly modified) P-wave (V_P) and shear-wave (V_S) velocity models used by Escobedo *et al.* (1998) to study the CJ 1995 earthquake and by Shapiro *et al.* (2000) to study wave-guide effects on Mexican subduction events.

Simulations by Shapiro *et al.* (2000) showed significant influence of a thin accretionary prism postulated for Mexico's subduction zone on the duration, the amplitudes, and the frequency content of the strong ground motions generated by seismic sources located near the prism. Based on these results, which were constrained by strong-motion data, we include models with and without the accretionary prism in our study (see Fig. 9). The maximum horizontal and vertical dimensions of the accretionary prism were 60 and 7 km, respectively (see Fig. 9). The thicknesses, V_P, V_S, and density values of the 6 layers included in the model, namely, (1) water, (2) the accretionary prism, (3) the upper continental crust, (4) the lower continental crust, (5) the oceanic crust, and (6) the upper mantle, are also listed in Figure 9.

The finite seismic source of the CJ 1995 earthquake was modeled by the four-subevent thrust source model proposed by Escobedo *et al.* (1998), as shown in Figures 2 and 8a. The surface projection of the location of the four subevents inside the (total) rupture area of 160 (length) $\times$ 90 (width) km^2 of the 1995 event are also shown in Figure 8b. The source parameters used in the LF modeling of the 1995 earthquake for the four subevents are presented in Table 1. The four source ruptures were kinematically simulated, radially propagating outward with a constant rupture velocity (V_r) and slip. Two different rupture velocities were used in the study, 2.2 and 2.6 km/s, in agreement with Escobedo *et al.* (1998), which found that the former value provided the minimum root-mean-square value (rmsv) errors between the observed and their synthetic seismograms, and the latter value corresponded to an intermediate value of their computed rmsv errors.

The slip rate function used for all sources was an isosceles triangle with a constant rise time of 1 s, following

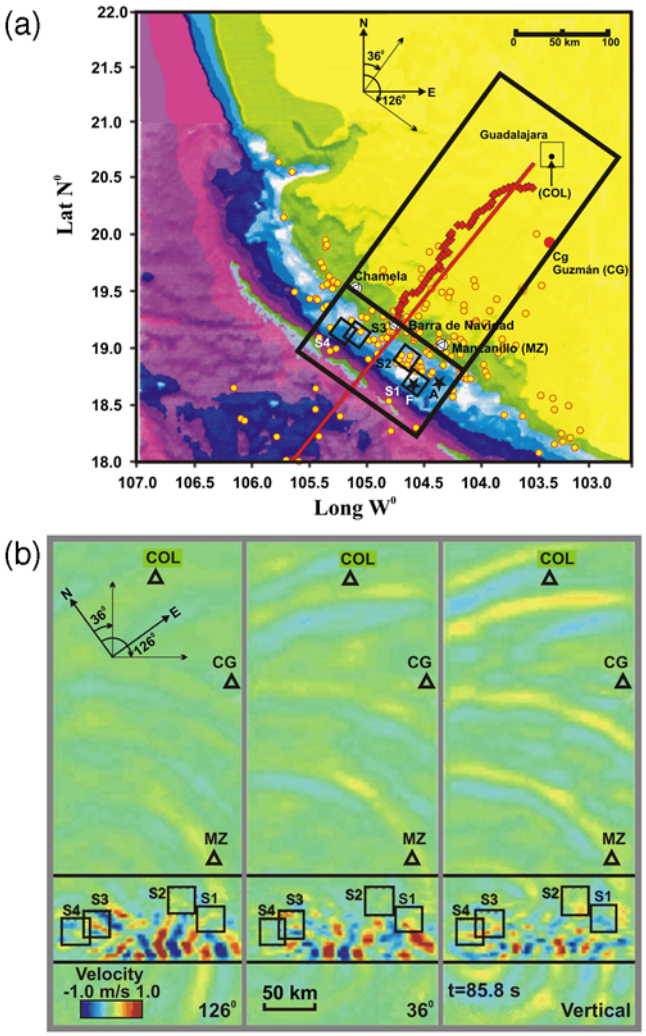

Figure 8. (a) Surface projection (large rectangle) of the 2.5D model (see Fig. 9) multiple subevent finite-difference simulation of the 9 October 1995 mainshock. The rupture area of the considered seismic source is depicted by the small rectangle. S1–S4 (small dashed squares) depict the location and dimension of the four subevents proposed by Escobedo *et al.* (1998) to represent the mainshock, F is the largest foreshock, and A is the largest aftershock (stars). (b) Surface velocity snapshots at time 85.6 s of the synthetic velocity wave-field propagation pattern, for frequencies <0.5 Hz along 126° and 36° as well as the vertical component. The color version of this figure is available only in the electronic edition.

Irikura (1998). However, the effective rise time is increased somewhat after low-pass filtering the LFs to 0.5 Hz. The average fault area for the four subevents was 45×45 km^2, which was computed by following Wells and Coppersmith (1994) equations relating rupture areas as a function of M_w for the four considered subevents (see Table 1; details of these calculations are presented in the HF modeling section). The focal mechanisms used in the modeling for the four subevents were purely thrust mechanisms (Fig. 2), as suggested by Escobedo *et al.* (1998), with strike parallel to the trench. Table 2 summarizes the numerical parameters as well as the minimum V_P, V_S and the densities of the considered geological layers.

Figure 8b shows snapshots, for a simulation time $t = 85.6$ s, of the two horizontal (along 126° and 36°) and vertical components of the long-period (≤ 0.5 Hz) 3D-surface synthetic velocity pattern ($V_r = 2.2$ km/s). Notice the long-period waves propagating in the intermediate field (station CG) and far field (station COL), compared with the higher-frequency waves trapped in the low-velocity layer of the accretionary prism (in the vicinity of the near-field station MZ).

In Figures 10 and 11a–l, we show the LF WE and NS synthetic accelerograms for stations MZ, CG, and COL and their corresponding Fourier amplitude spectra, generated with and without the accretionary prism (see Fig. 9) for rupture velocities $V_r = 2.2$ km/s and $V_r = 2.6$ km/s, respectively, associated with the ruptures of subevents S1–S4 (see Fig. 8a). The PGA obtained for MZ in the WE direction from the synthetics generated by the model with the accretionary prism is more than three times that from the model without the accretionary prism, and in the NS direction, the PGAs are very similar, Figure 10a,c, respectively. The corresponding Fourier amplitude spectra show a similar pattern in the maximum amplitudes for frequencies between 0.1 and 0.5 Hz (Fig. 10b,d). The large amplitudes and high-frequency content of the synthetic accelerograms of the model including the accretionary prism are associated with trapped waves in the latter, as shown in Fig. 8b. The PGA and maximum Fourier amplitude spectra of the LFs from the model including the accretionary prism are about twice those derived from the model without the accretionary prism for station CG (see Fig.. 10e,g and f,h, respectively). At COL, the PGA obtained from the model with the accretionary prism is about 30% larger than that from the model without the prism (Fig. 10i,k); the maximum Fourier amplitude spectra for the model with the accretionary prism are also larger than those for the model without the prism, particularly for frequencies between 0.2 and 0.5 (Fig. 10j,l). From these results, we conclude that the model with the accretionary prism generates larger amplitudes at higher frequencies on the LF synthetics, compared with the synthetics associated with a geological structure without the accretionary prism. This effect diminishes with the hypocentral distance to the stations. In general, the Fourier amplitude spectra from LF synthetics generated by the model including the accretionary prism are in better agreement with the data as compared to those generated from the model without the accretionary prism (see Fig. 10b,d,f,h,j,l). Notice that for $V_r = 2.6$ km/s (Fig. 11a–l), the differences between the observed Fourier amplitudes and those corresponding to the synthetic seismograms are in general larger than the differences obtained for $V_r = 2.2$ km/s. Thus, in the rest of our study, we use the LF results for $V_r = 2.2$ km/s shown in Figure 10a–l.

High-Frequency Synthetics

To generate the HF synthetics (>0.5 Hz) of the 9 October 1995 earthquake, we applied Irikura's (1986) version of

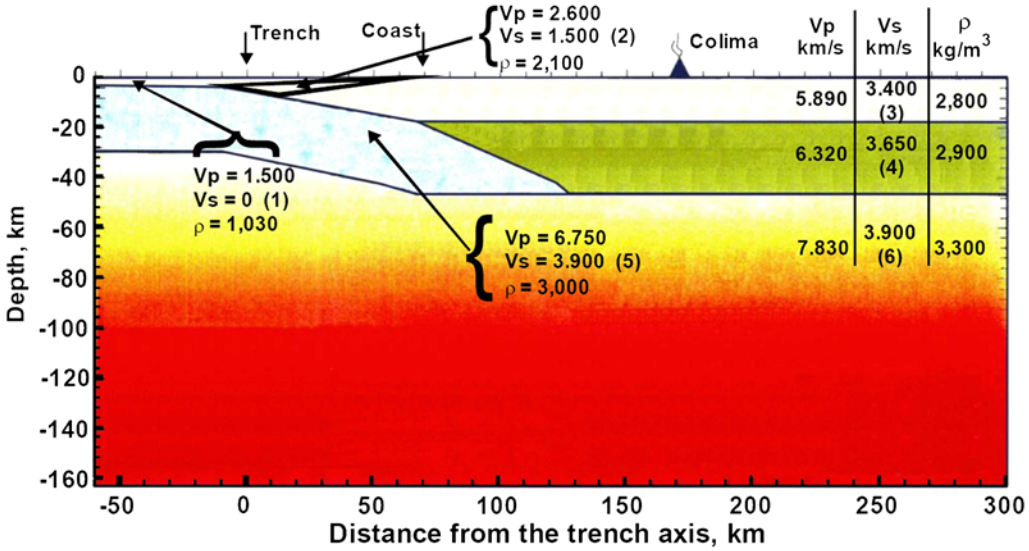

Figure 9. 2.5D model used in the finite-difference simulations. V_P (km/s), V_S (km/s), and ρ (km/s^3) of the considered layers: (1) water, (2) the accretionary prism, (3) the upper continental crust, (4) the lower continental crust, (5) the oceanic crust, and (6) the upper mantle (modified from Bandy *et al.*, 1999; Escobedo *et al.*, 1998; Shapiro *et al.*, 2000). The color version of this figure is available only in the electronic edition.

the EGF technique. Following this technique, the ground motions for the mainshock are generated by the superposition of those obtained through the largest foreshock and aftershock for each of the four subevents representing the mainshock (as proposed by Escobedo *et al.*, 1998). For the surficial geological layers in the CJ region, particularly nearby stations CG and COL (Campos–Enriquez and Alatorre–Zamora, 1998), we used an average V_S value of 3.09 km/s and a V_r of 2.2 km/s, in agreement with the findings of Escobedo *et al.* (1998). The seismic source parameters are summarized in Table 1.

As mentioned in the High-Frequency Modeling section, the accelerograms recorded at stations MZ, CG, COL surface, and COL rock for the F and A events (shown in Fig. 5) were used as the EGF time series, $u(t)$, required in equation (1). Notice that the epicentral location of the F and A events are a few tens of kilometers from those corresponding to the subevents 1 and 2, and ~100 km from the location of subevents 3 and 4 (see Fig. 2). These subevents started rupturing at 0, 13.8, 29.4, and 44 s, respectively (see Escobedo *et al.*, 1998). It is also important to mention that there are no recordings available at MZ, CG, COL surface, and COL rock stations for other (smaller magnitude than F and A) foreshocks or aftershocks of the event with epicenters located nearby S1–S4.

Table 2
Parameters for the Low-Frequency 2.5D Modeling of the 9 October 1995 M_w 8 Earthquake

Parameters	Value
Spatial discretization (m)	600
Temporal discretization (s)	0.035
P-wave minimum velocity (kg/s) (water/crust)	1500/2600
S-wave minimum velocity (kg/s) (water/crust)	0/1500
Minimum density (kg/m^3)	1030
Number of grid points 126° direction	273
Number of grid points 36° direction	591
Number of grid points vertical direction	272
Number of time steps	7143
Simulation time (s)	250

Taking the mentioned recording data restrictions into account, for the generation of the HF synthetics at MZ, CG, and COL stations, the following selection of the available F and A recordings was made to represent the EGF of the S1–S4 sources: (1) for the near-field station MZ, the records of the A and F events (Fig. 5) were used to represent the EGFs of S1 and S2. S3 and S4 were omitted due to the lack of foreshock and aftershock recordings with nearby epicenters as well as because the WE and NS components of the recordings of the mainshock at MZ showed small amplitudes after 30 and 40 s, in other words, when the contribution of S3 and S4 in the HF simulation would start. Note that we computed the MZ-station HF synthetics with the four subevents and obtained unsatisfactory results, as shown in the Ⓔelectronic supplement to this paper. (2) For station CG, which is located in the intermediate field, the only available records are the ones from the F event; therefore, those records were used as EGFs to compute the synthetics of S1–S4. (3) For stations COL_{rock} and $COL_{surface}$ (located in the far field), the records associated with the A and F events were used as EGFs for the four subevents.

To obtain the N elementary sources associated with each of the S1–S4, equation (4) was applied with the M_0 of the considered subevent and with the m_0 value corresponding to the F or A events (depending on the subevent and the A or F, under consideration). An average value of $C = 1.60$ was used, accordingly with Gibowicz's (2004) suggestion about

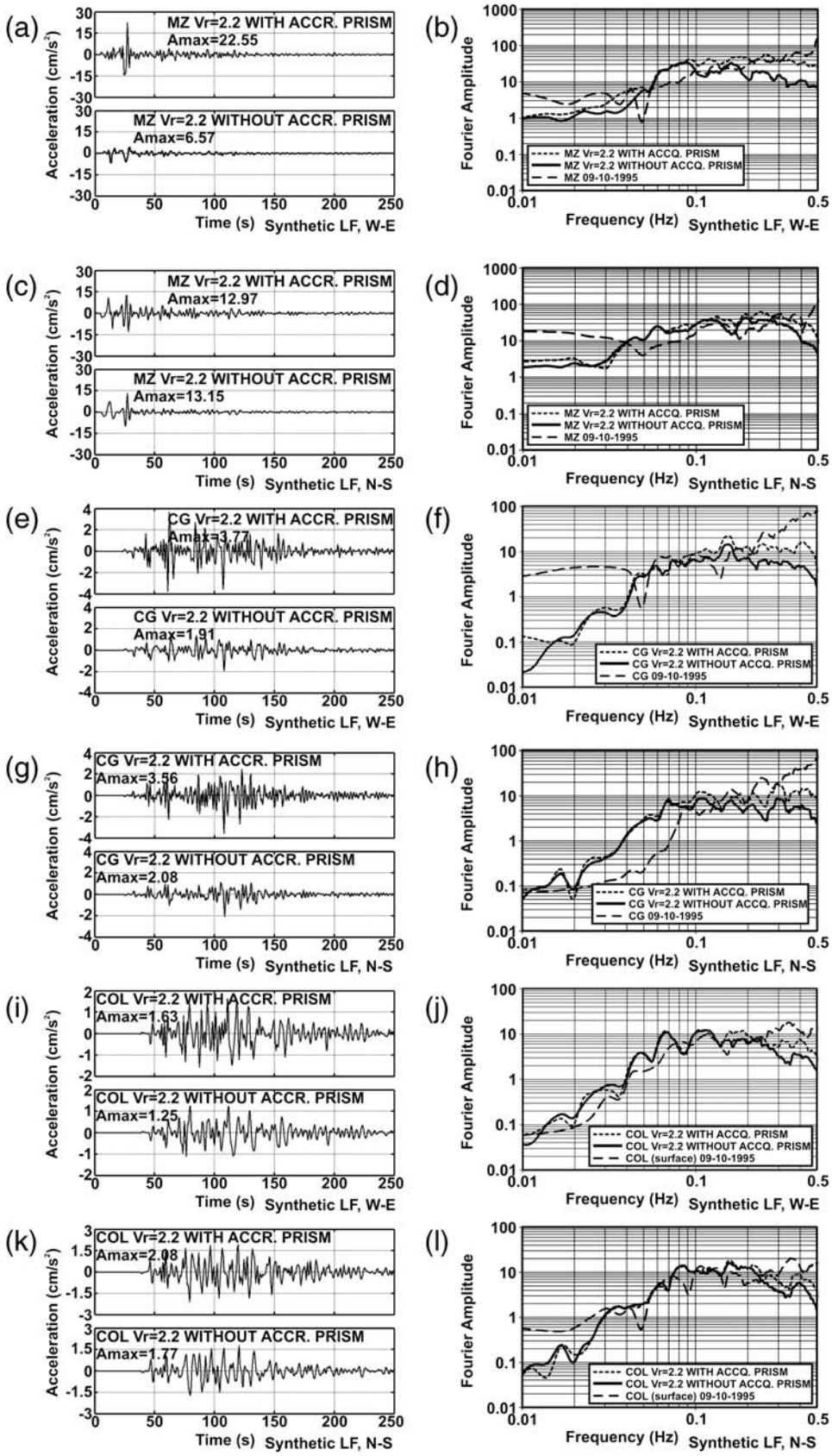

Figure 10. Left, LF synthetics on WE and NS components, with and without the accretionary prism for $V_r = 2.2$ km/s (see Fig. 8), associated with subevents S1–S4 (see Fig. 8) of the 9 October 1995 earthquake for stations (a,c) MZ, (e,g) CG, and (i,k) COL. Right, Fourier amplitude spectra of the LF synthetic acelerograms for stations (b,d) MZ, (f,h) CG, and (j,l) COL.

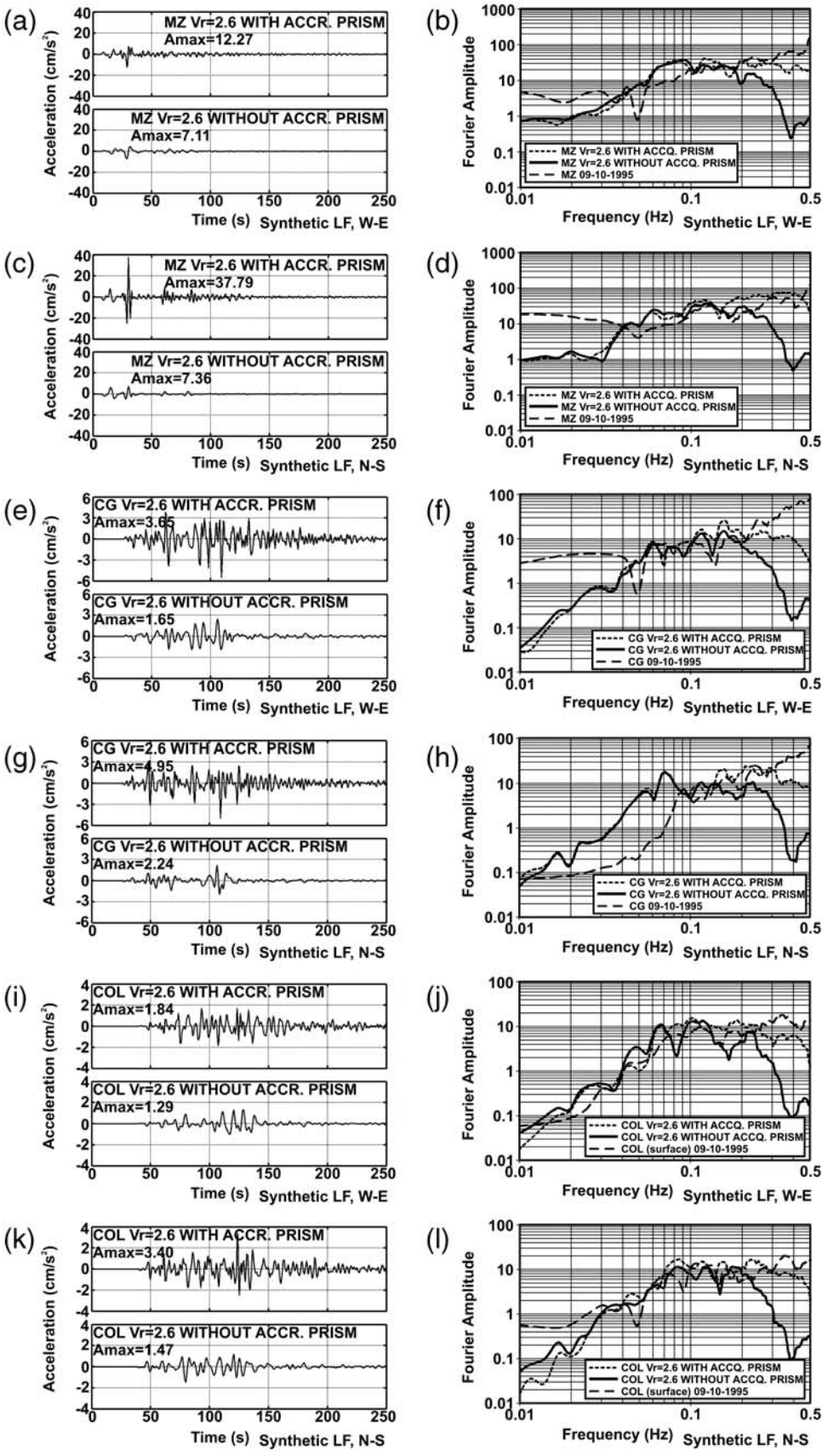

Figure 11. Same as Figure 10 but for $V_r = 2.6$ km/s (see Fig. 8).

the average stress release ratio of large-magnitude earthquakes and their largest aftershocks. Gibowicz's (2004) results were obtained from a worldwide 65 sample data of sequences of earthquakes that occurred from 1977 to 1997, including the 9 October 1995 M_w 8 CJ event (and the Oaxaca, Mexico, 1978 M_w 7.6 and the Petatlan, Mexico 1979, M_w 6.9 events). By inserting the corresponding M_0 and m_0 values of Table 1 into equation (4), we obtained N equal to 4 for S1–S4.

The rupture areas A_0 of S1–S4 (Table 1) were computed following Wells and Coppersmith's (1994) equation for thrust events, in other words, $\log S = 0.98\ M_w - 3.99$ with $\sigma_{\log S} = 0.26$, for the mean plus one standard deviation. The M_w of S1–S4 were calculated by the Kanamori and Anderson (1975) equation, $M_w = (\log M_0/1.5) - 10.73$. From the application of those equations, the A_0 values obtained for S1–S4 were 1995, 2137, 1905, and 2187 km^2, respectively. We then estimated the elementary source area (a_0) from Frankel (1995) as well as Hartzell *et al.* (1999) as $a_0 = (m_0/M_0)^{2/3} A_0$ for S1–S4 and obtained 133, 132, 133, and 134 km^2, respectively, for the A event, and 90, 89, 89, and 90 km^2, respectively, for the F event. The rise time τ of equation 3 was estimated at ~1.3 s for the four subevents by applying the expression $\tau = 1.72 \times 10^{-9} (M_0)^{1/3}$ proposed by Irikura (1998). Finally, in equation 3, $n' = 100$ was used.

The HF synthetics associated with the four subevents were combined, taking into account the time lag between the start of the ruptures of their respective seismic sources suggested by Escobedo *et al.* (1998), in other words, 0, 13.8, 29.4, and 44 s, and the hypocenter locations of S1–S4 with respect to the MZ, CG, and COL stations (see Figs. 2, 3, and 8).

In Figures 12, 13, and 14 a,g and b,h, the WE and NS components of the HF synthetics for stations MZ, $COL_{surface}$ and COL_{rock}, respectively, obtained with the F and A recordings of the CJ 1995 mainshock as the EGF of equation (1) are shown. The corresponding results for station CG are shown in Figure 15a,b, for the WE and NS directions, respectively (synthetics corresponding only to the F records available in CG). Notice in Figures 12–15 that for the near-field station MZ, the contribution from the S1 source to the amplitudes of the HF synthetics is about twice that from source S2. However, for the far ($COL_{surface}$, COL_{rock}) and intermediate (CG) field stations, respectively, the contribution of the four sources (S1–S4) to the amplitudes of their respective HF synthetics are of the same order. Also note in Figures 12–14 that the maximum amplitudes and the durations of the HF synthetics obtained with the F recordings (used as EGFs) for stations MZ, $COL_{surface}$ and COL_{rock} are larger than the corresponding ones computed with the A recordings as EGFs.

Synthesis of the Low- and High-Frequency Synthetics

The LF and HF synthetics shown in Figures 10 and 12–15, respectively, were combined using matched filters at a frequency f_m. The following procedure was carried out to obtain the BB synthetics. First, the Fourier amplitude spectra of both LF ($\leq f_m$) and HF ($> f_m$) synthetics were computed, after which a spectral weighting function was applied to each of the amplitude spectra. For the LF synthetics, the weighting function was one from 0.01 to f_m Hz, tapering to zero from f_m to a maximum specified frequency of f_n Hz ($f_n > f_m$) as a one-sided Hanning window. Similarly, the weighting function for the HF synthetics was applied from f_m to 10 Hz, tapering to zero from f_m to f_l ($f_l < f_m$) as a one-sided Hanning window. Next, the BB synthetic was computed by adding the filtered LF and HF spectra and obtaining its inverse Fourier transform.

The matching frequency f_m to filter the LF and HF synthetics was chosen taking into account that the Fourier amplitude spectral fall-off of the LF synthetics starts at ~0.4 Hz (see Fig. 10b,d,f,h,j,l). Moreover, the energy content of the foreshock and aftershock of the 1995 CJ earthquake, which were used as EGFs, start increasing at ~0.4 Hz (see Fig. 6). Therefore, we selected $f_m = 0.4$ Hz and the tapering frequencies $f_n = 0.5$ Hz and $f_l = 0.3$ Hz for the LF and HF synthetics, respectively.

In Figures 12, 13, and 14c,i and d,j, we show the WE and NS components of the matched-filtered LF and HF and the BB synthetic accelerograms for stations MZ, $COL_{surface}$ and COL_{rock}, respectively, obtained with the F and A recordings of the CJ 1995 mainshock as the EGF of equation (1) are shown, respectively. The corresponding results for station CG are shown in Figure 15c,d for the WE and NS directions, respectively.

Finally, in Figures 12–14e,k and f,l, the WE and NS components of the observed and the BB synthetic accelerograms for stations MZ, $COL_{surface}$ and COL_{rock}, obtained with the F and A recordings of the CJ 1995 mainshock as the EGF of equation (1) are shown, respectively. The corresponding results for station CG are shown in Figure 15e,f for the WE and NS components, respectively.

The corresponding Fourier amplitude spectra of the observed and BB synthetic accelerograms of Figures 12–15 are shown in Figure 16 (the filtered LF and HF, as well as the respective hybrid Fourier amplitude spectra for the MZ, $COL_{surface}$, COL_{rock}, and CG stations are included in Ⓔthe electronic supplement to this paper). Notice in these figures that in general, the agreement between the shapes and amplitudes of the Fourier spectra for the observed and synthetic spectra are reasonable for the near-field (MZ), intermediate-field (CG), and far-field (COL) stations in the frequency band analyzed (0.01–10 Hz). In particular, the Fourier amplitudes for the low and high frequencies of the BB synthetics and data are similar, while the largest discrepancies are found for the intermediate frequencies. However, notice that the local site effects for the stations MZ (observed from 0.5 to 0.9 Hz), $COL_{surface}$ (occurring from 1.5 to 4 Hz; Chavez 1995, 2000) and CG, (identified from 0.3 to 0.9 Hz), are well reproduced by the synthetics (see Fig. 16).

The response spectra for a critical damping of 5% of the observed and BB synthetic accelerograms of Figures 12–15

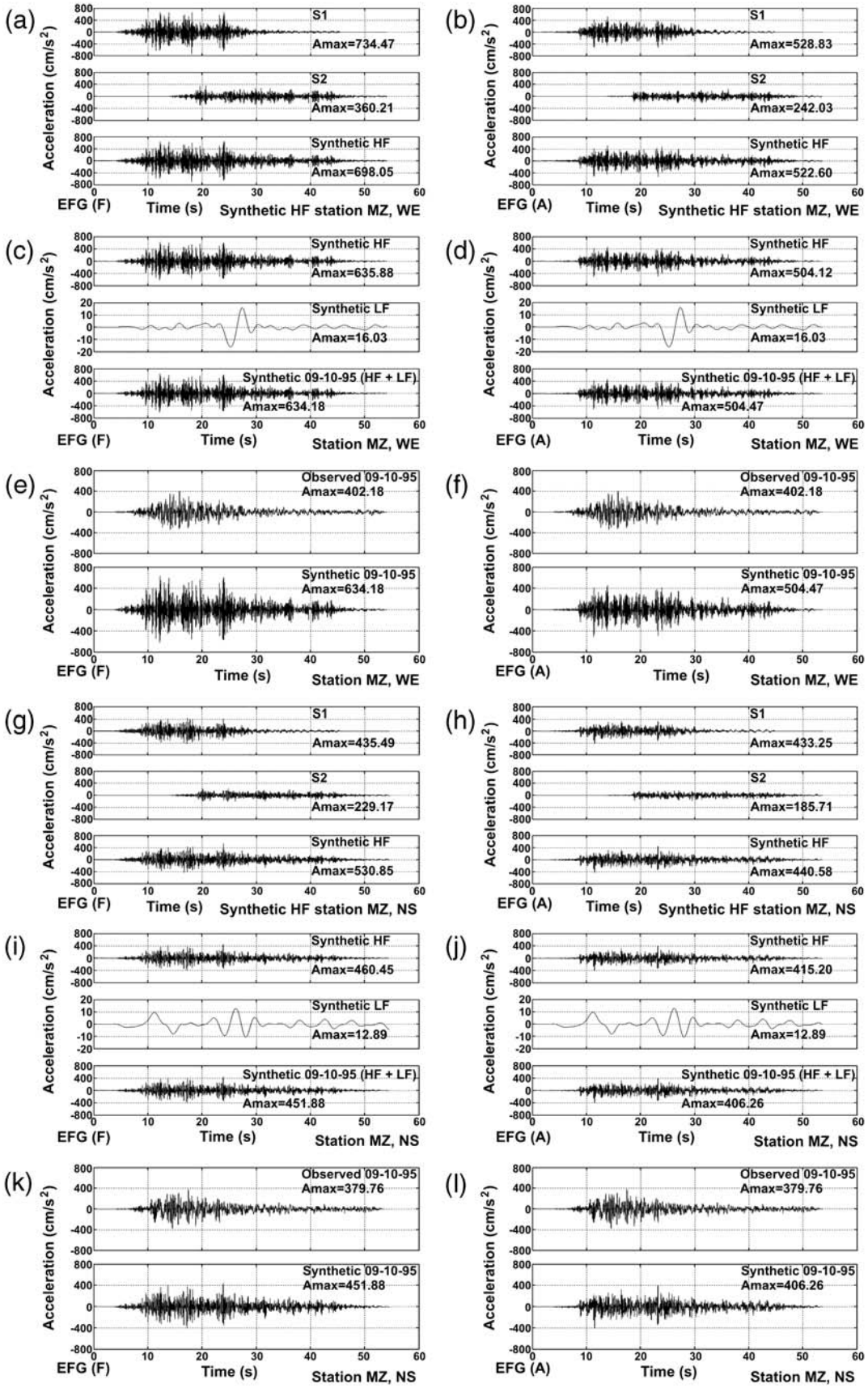

Figure 12. Broaband seismograms at station MZ. (a,b and g,h) HFs, (c,d and i,j) LFs, and (c,d and i,j) BBs. (e,f and k,l) Comparisons of WE and NS, respectively, observed and BB synthetics, associated with S1–S4 (see Fig. 8) for the 9 October 1995 earthquake.

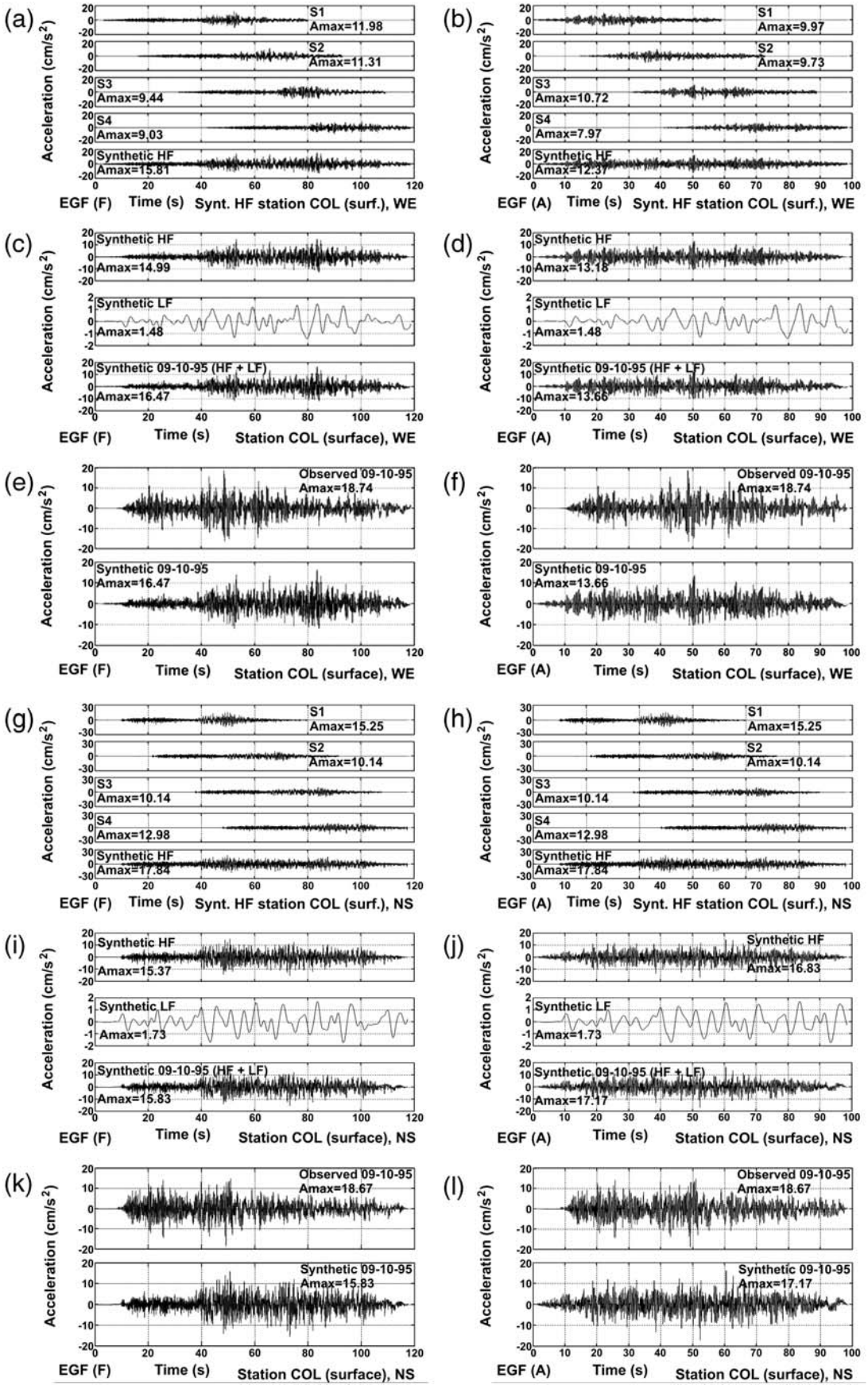

Figure 13. Same as Figure 12, but for station $COL_{surface}$.

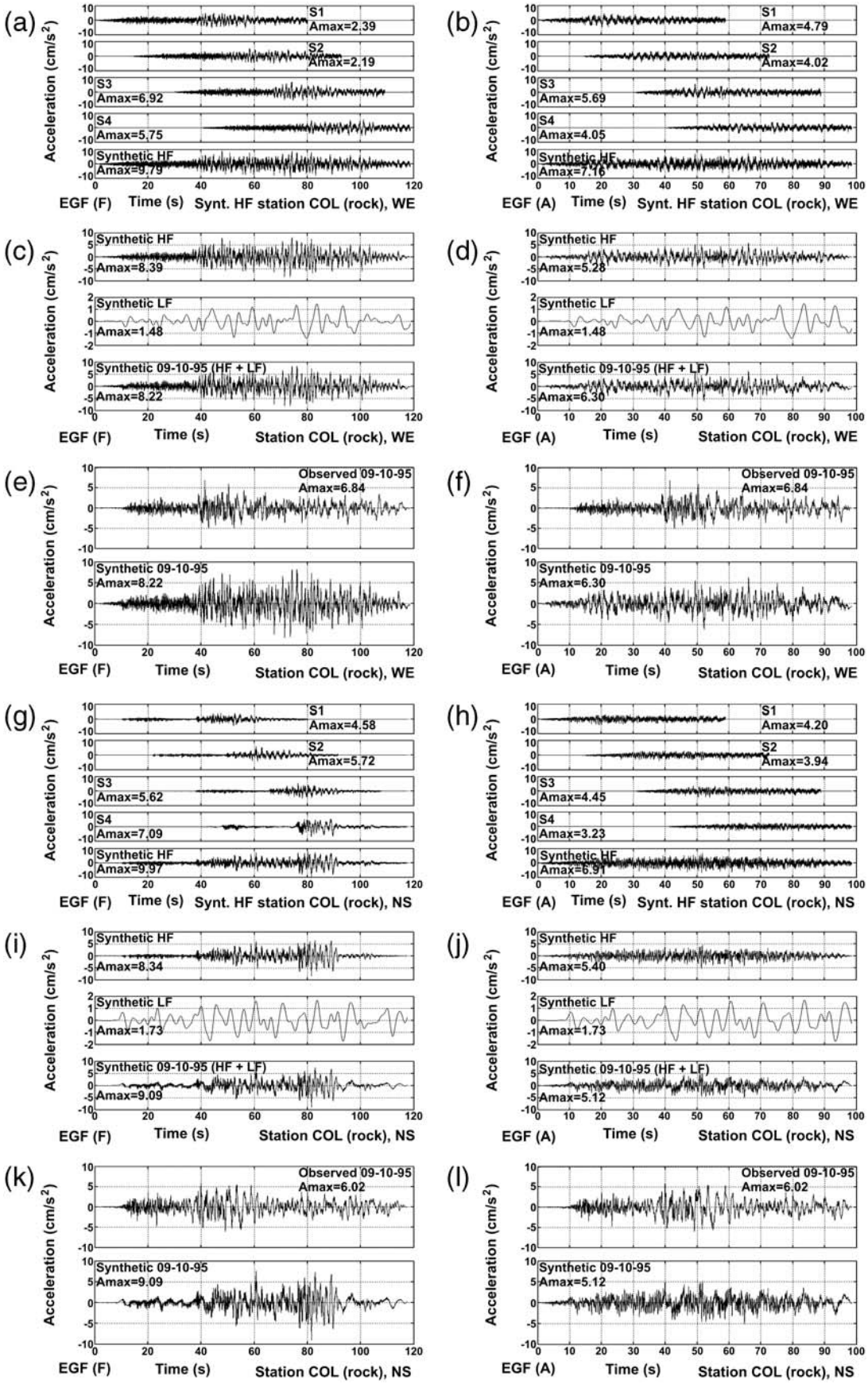

Figure 14. Same as Figure 12, but for station COL_{rock}.

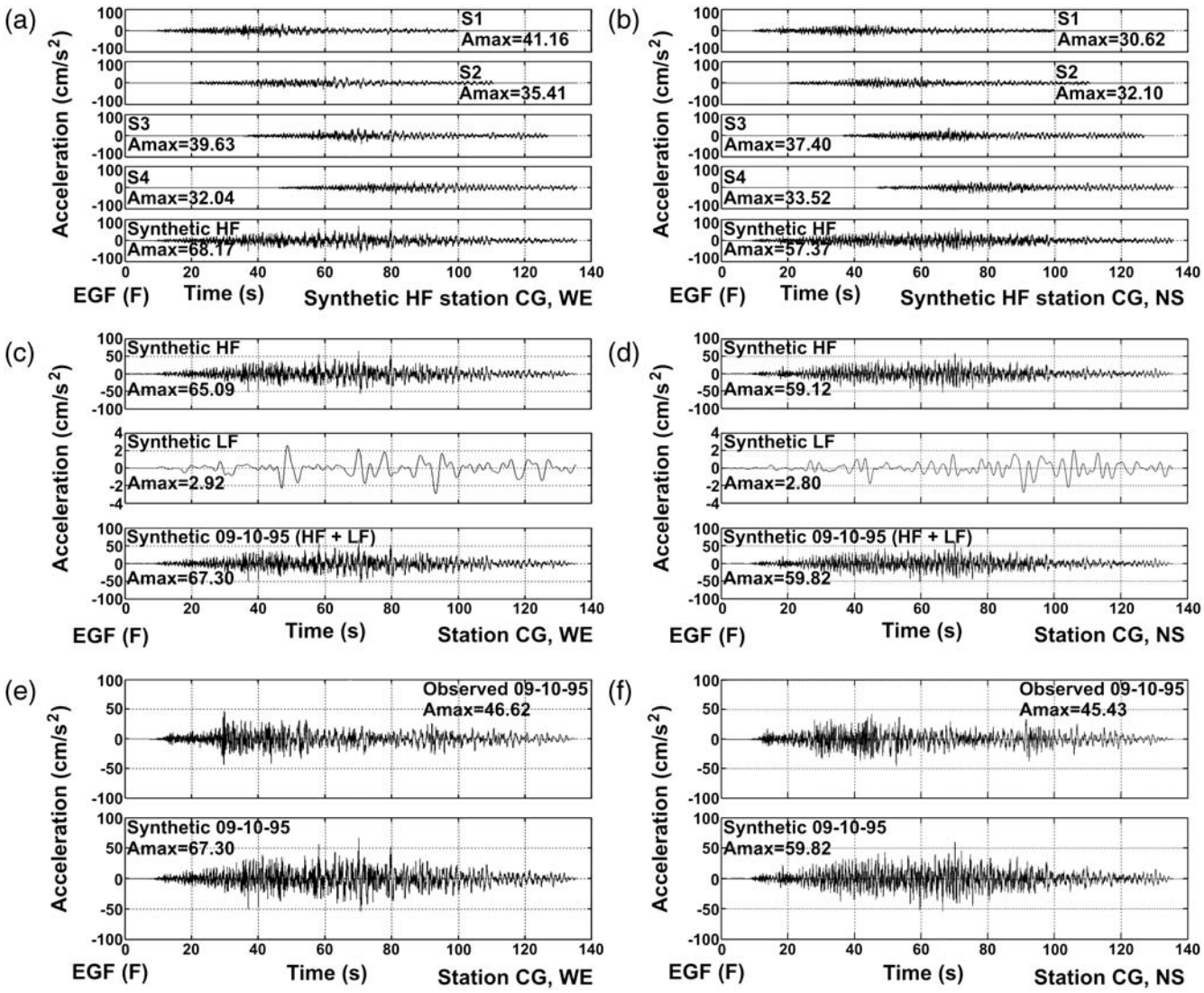

Figure 15. Same as Figure 12, but for station CG.

are shown in Figure 17. The agreement between the response spectra for the observed and synthetic spectra are, as a whole, reasonable for the near-field (MZ), intermediate-field (CG) and far-field (COL) stations in the frequency band analyzed (0.01–10 Hz). In particular, the response spectral amplitudes for periods between 0.01 and ~1 s of the BB synthetics and data are similar, especially for the synthetics computed with the aftershock (*A*) recordings. The largest discrepancies are found for periods >~1 s. However, notice that the local site effects for the stations MZ (observed at ~0.3 s in the NS components), $COL_{surface}$ (occurring at ~0.4 s; Chavez 1995, 2000), and CG, (identified at ~0.2 and 0.3 s), are well reproduced by the synthetics (see Fig. 17).

Discussion and Conclusions

The CJ region of northwestern Mexico is prone to the occurrence of destructive large-magnitude subduction earthquakes such as the M_S 8.2 of 3 June 1932 and the M_w 8 of 9 October 1995, and it is a region in which there is a scarce seismological infrastructure, particularly for engineering purposes of strong ground motion recordings for the earthquakes. This situation makes the assessment of reliable estimates of the seismic hazard particularly difficult for sites located in the CJ region. However, the accelerographic network of the metropolitan zone of Guadalajara (whose 13 stations included the $COL_{surface}$ and COL_{rock} stations) and the station CG were deployed in the early 1990s (Chavez, 1993, 1995), and they recorded the 1995 mainshock and its largest foreshock and aftershock of the 6 and 12 October.

Our analysis of the time and frequency content of strong ground-motion records at stations MZ (near field), CG (intermediate field), $COL_{surface}$ (far field) and COL_{rock} (far field) shows that, except for a magnitude-related scale factor, the source, path, and respective local effects associated with the M_w 8 mainshock, the largest foreshock (M_w 5.75) and aftershock (M_w 5.92) of the CJ 9 October 1995 earthquake

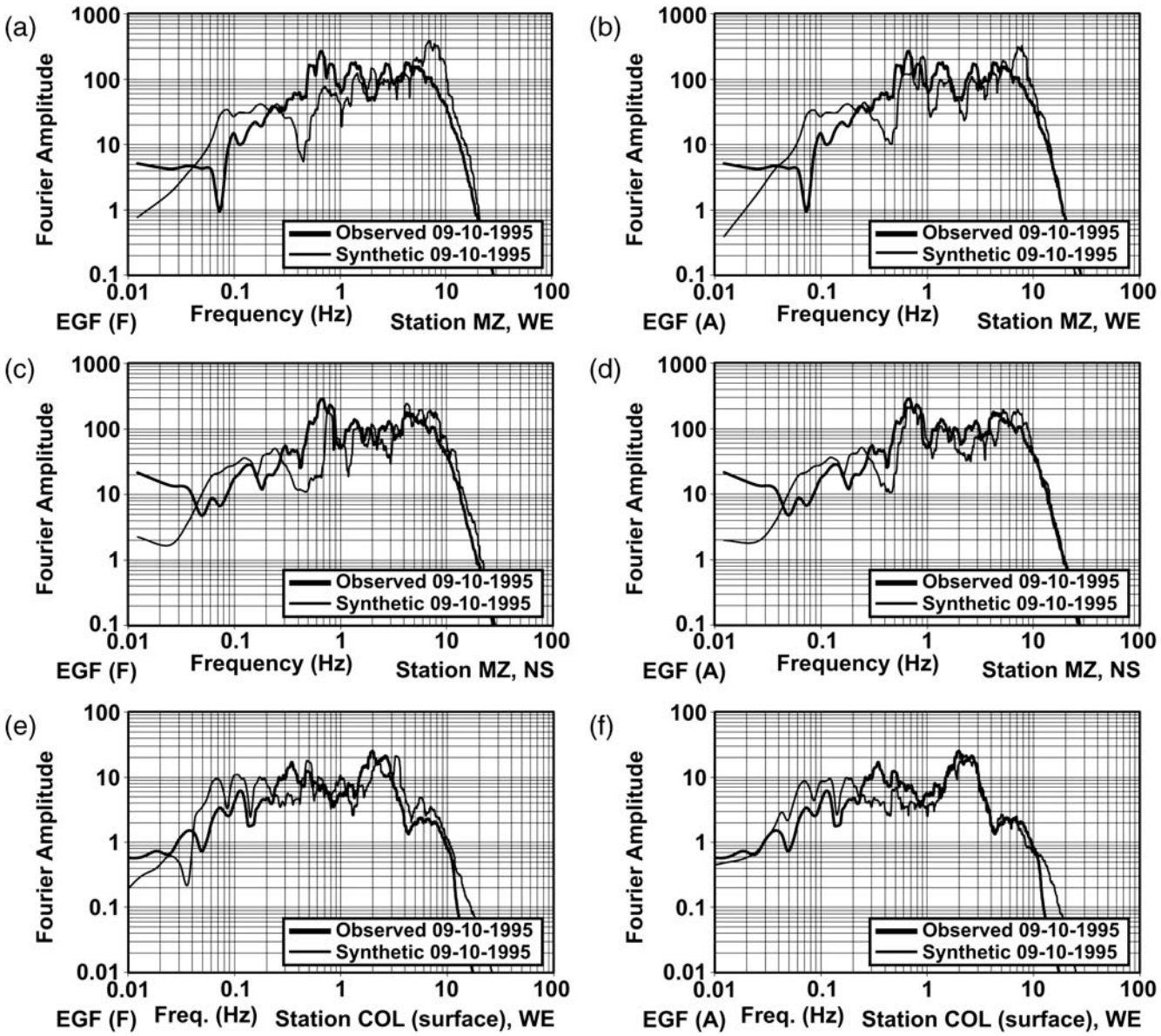

Figure 16. Comparison of the Fourier amplitude spectra of acceleration of the observed (thick continuous line) and BB synthetics (thin continuous line) for stations (a–d) MZ, (e–h) $COL_{surface}$, (i–l) COL_{rock} and (m,n) CG for the 9 October 1995 earthquake. (*Continued*)

are similar. We applied a hybrid method to generate BB synthetic (0.01–10 Hz) ground motions at MZ, CG, and COL for the mainshock; this method combines long-period ($\leq$0.5 Hz) finite-difference simulations and HF ($>$0.5 Hz) synthetics obtained by the EGF technique. The LF synthetics were simulated using a finite-fault (four subevents) description of the CJ 1995 earthquake seismic source and a 2.5D structural model constrained by gravity and seismological data from the modeled physical volume. The HF synthetics were modeled from the recordings of the largest foreshock and aftershock at MZ, CG, and COL, and the same finite-fault description was used for the LF modeling.

The comparisons in the time and frequency domain (including the response spectra for 5% critical damping) of the synthetics with the observed strong ground motions for the 1995 earthquake in the near field (MZ), intermediate field (CG), and the far field ($COL_{surface}$ and COL_{rock}) are generally satisfactory. The match is facilitated by including an approximation of the accretionary prism in the subduction zone, which increases the spectral amplitudes to a level in better agreement with the strong-motion data, as compared to our models without the accretionary prism.

In order to further analyze the differences between the observed and BB synthetic accelerograms for the four stations, we computed the coherence functions between the simulations and data (included in the available Ⓔelectronic supplement to this paper). This function provides a measure of the correlation of those time signals at each frequency of interest and varies from 0 (uncorrelated signals) to 1 (fully correlated), and allows a comparison of the amplitudes and

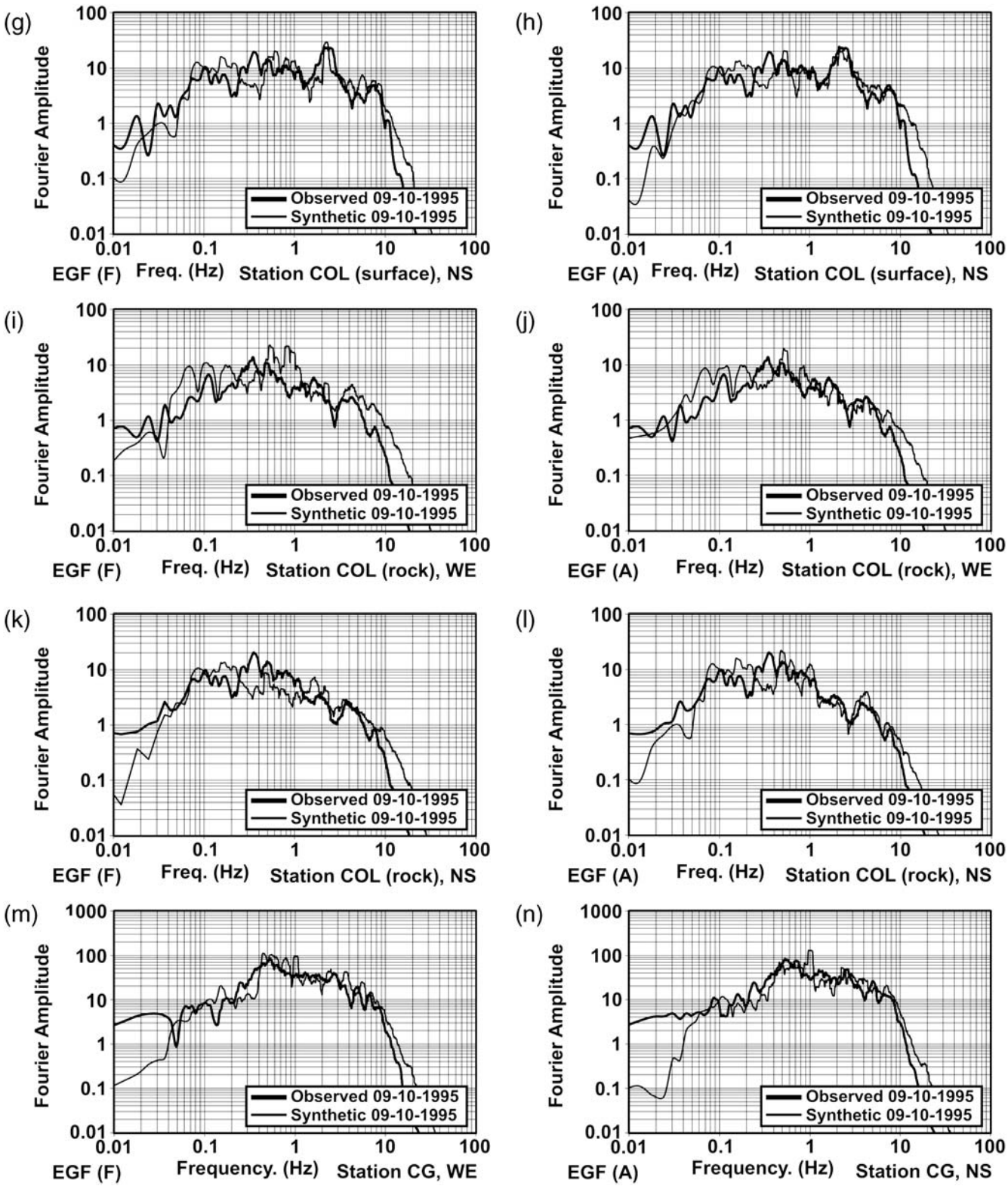

Figure 16. Continued.

the phase differences of the accelerograms simultaneously. If we consider that an arbitrary coherence value larger than 0.5 is acceptable for seismic hazard applications and consider in our analysis the coherences obtained with the HF synthetics of the aftershocks (A), the BB synthetics can be improved at the MZ station for frequencies < 0.08 Hz and 0.45–0.75 Hz, at the CG station for frequencies 0.18–0.40 and 0.8–1.3 Hz, at $\mathrm{COL}_{\mathrm{rock}}$ for frequencies < 0.07 and 0.40–0.6 Hz, and at

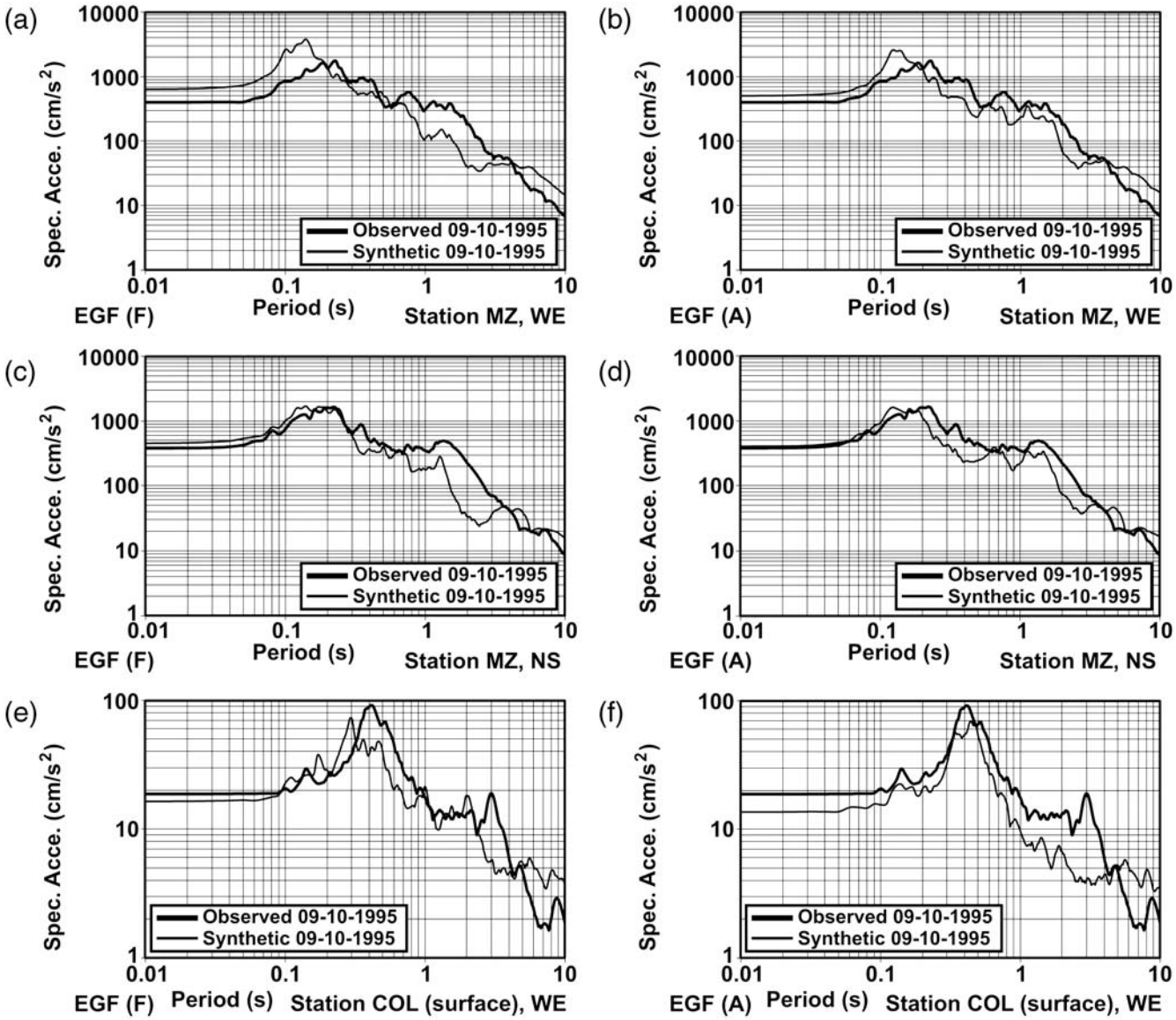

Figure 17. Comparison of the response spectra for a critical damping of 5% of the observed (thick continuous line) and BB synthetics (thin continuous line) for stations (a–d) MZ, (e–h) $COL_{surface}$, (i–l) COL_{rock} and (m,n) CG for the 9 October 1995 earthquake.(*Continued*)

$COL_{surface}$ station for frequencies 0.09–0.11 Hz, 0.12–0.18 Hz, and 0.3–0.65 Hz.

Taking into account the available earthquake recordings in the CJ region and the satisfactory synthetic results at MZ, CG, and COL for the M_w 8 CJ 9 October 1995 earthquake, we believe that our hybrid method is a first step towards the generation of more reliable estimates of the seismic hazard in regions such as the CJ. There is obviously some room for improvement; for example, we believe that a more realistic representation of the kinematic rupture process of the 1995 CJ earthquake (including variable rupture velocity and rise time, which becomes more important as the frequency of the LFs is increased) as well as of the surficial layering of the geologic model could lead to more accurate BB synthetics, in particular, for the intermediate frequencies. We leave this task for future work. We also strongly recommend the redeployment of the accelerographic network of Jalisco, particularly at Guadalajara, as well as deployment of a large number of seismological and accelerographic stations in the whole CJ region in order to increase the observational earthquake data in an area of Mexico, where potentially destructive extreme-magnitude M_w 8+ subduction earthquakes have been occurring at least since 1800 and up to 1995.

Data and Resources

We used strong-motion data from the near-field station MZ had a DCA-333R Terra Technology accelerograph operated by the Centro de Instrumentación y Registro Sísmico A.C. (CIRES) on behalf of the Comision Federal de Electricidad of Mexico. Strong-motion data was also included for the intermediate-field (CG) and far-field ($COL_{surface}$ and

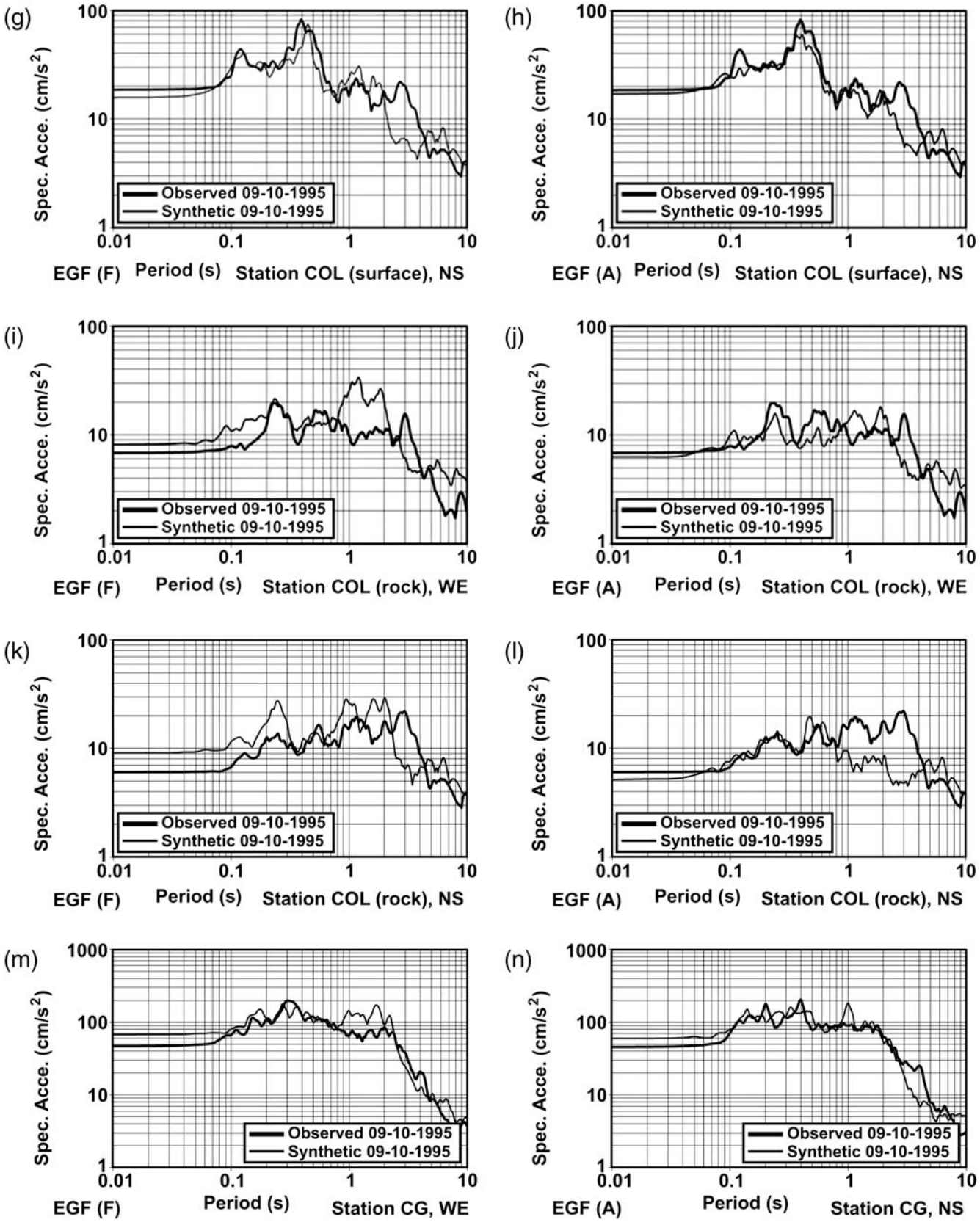

Figure 17. Continued.

COL_{rock}) stations, which were part of the JAN (equipped with SSA-2 Kinemetrics instruments) installed in 1992–1993 in the state of Jalisco to monitor the strong ground motions in the second largest city of Mexico (Guadalajara) where 11 free-field and two downhole stations were deployed (Chavez, 1993, 1995) and one free-field station in the second largest town (Ciudad Guzman) of the state of Jalisco (see Fig. 3).

The low-frequency computations in this study were carried out at Dirección General de Servicios de Cómputo Académico—Universidad Nacional Autonóma de México (DGSCA-UNAM).

Acknowledgments

We thank J. Saborío O., D. Almora, J. M. Velazco, Ricardo Vazquez, Rodrigo Ramirez, and Alicia Martinez for their participation in the different stages of the planning, the performance of ambient vibration tests in Guadalajara and Ciudad Guzman, and the deployment, maintenance, and operation of the JAN up to 1997. Thoughtful reviews from anonymous reviewers significantly improved the manuscript. We acknowledge DGSCA-UNAM for allowing us to use their supercomputer facilities.

References

Bandy, W., V. Kostoglodov, H. Hurtado-Díaz, and M. Mena (1999). Structure of the southern Jalisco subduction zone Mexico, as inferred from gravity and seismicity, *Geofis. Int.* **38,** no. 3, 127–136.

Campos-Enriquez, J. O., and M. A. Alatorre-Zamora (1998). Shallow crustal structure of the junction of the grabens of Chapala, Tepic-Zacoalco and Colima Mexico, *Geofis. Int.* **37,** 263–282.

Cerjan, Ch., D. Kosloff, R. Kosloff, and M. Reshef (1985). A nonreflecting boundary condition for discrete acoustic and elastic wave equations, *Geophysics* **50,** no. 4, 707–708.

Chavez, M. (1993). Red acelerográfica de la zona metropolitana de Guadalajara (RAZMG), SMIS, Mexico, Memorias X Congreso Nacional de Ingeniería Sísmica, 294–300.

Chavez, M. (1995). Geotechnic, hazard and seismic safety of the Metropolitan zone of Guadalajara, Mexico, Invited opening conference, *X Panam. Conf. Soil Mech. Found. Eng.*, Guadalajara, Mexico, Vol. 4, 33–93.

Chavez, M. (2000). Impact of the local geology on the seismic vulnerability of the metropolitan zone of Guadalajara, Mexico, *Twelfth World Conf. Earthq. Eng.*, Auckland, New Zealand, 30 January–4 February, CD-Paper 1600.

Escobedo, D., J. F. Pacheco, and G. Suarez (1998). Teleseismic body-wave analysis of the 9 October, 1995 ($M_w = 8.0$), Colima-Jalisco, Mexico earthquake, and its largest foreshock and aftershock, *Geophys. Res. Lett.* **25,** no. 4, 547–550.

Frankel, A. (1995). Simulating strong motions of large earthquakes using recordings of small earthquakes: The Loma Prieta mainshock as a test case, *Bull. Seismol. Soc. Am.* **85,** no. 4, 1144–1160.

Gibowicz, S. J. (2004). Stress release during earthquake sequences, *Acta Geophys. Polonica* **52,** no. 3, 271–299.

Graves, R., and A. Pitarka (2004). Broadband time history simulation usinga hybrid approach, *World Conf. Earthq. Eng.*, Vancouver (British Columbia), Canada, August 1–6, 2004, paper No. 1098.

Gottschaemmer, E., and K. B. Olsen (2001). Ground motion synthetics for spontaneous versus prescribed rupture on a 45° thrust fault, American Geophysical Union, Fall Meet. 2001, abstract #s42c-0667.

Hartzell, S. H. (1978). Earthquake aftershocks as Green's functions, *Geophys. Res. Lett.* **5,** 1–4.

Hartzell, S., S. Harmsen, A. Frankel, and S. Larsen (1999). Calculation of broadband time histories of ground motion: Comparison of methods and validation using strong-ground motion from the 1994 Northridge earthquake, *Bull. Seismol. Soc. Am.* **89,** no. 6, 1484–1506.

Heaton, T., and S. Hartzell (1986). Source characteristic of hypothetical subduction earthquakes in the northwestern United States, *Bull. Seismol. Soc. Am.* **76,** 675–708.

Irikura, K. (1986). Prediction of strong acceleration motion using empirical Green's function, *Proc. Seventh JEES*, 151–156.

Irikura, K. (1998). Prediction of strong motions from future earthquakes in Osaka basin, *Proc. Second Int. Symp. "The effects of Surface Geology on Seismic Motion"*, A. A. Balkema 1, 171–188.

Kamae, K., K. Irikura, and A. Pitarka (1998). A technique for simulating strong ground motion using hybrid green's function, *Bull. Seismol. Soc. Am.* **88,** no. 6, 357–367.

Kanamori, H., and D. L. Anderson (1975). Theoretical basis of some empirical relations in seismology, *Bull. Seismol. Soc. Am.* **65,** 1073–1095.

Klitgord, K., and J. Mammerickx (1982). Northern East Pacific Rise: Magnetic anomaly and bathymetric framework, *J. Geophys. Res.* **87,** 6725–6750.

Kostoglodov, V., and W. Bandy (1995). Seismotectonic constraints on the convergence rate between the Rivera and North American plates, *J. Geophys. Res.* **100,** 17,977–17,989.

Liu, P., R. J. Archuleta, and S. H. Hartzell (2006). Prediction of broadband ground motion time histories: Hybrid low/high-frequency method with correlated random source parameters, *Bull. Seismol. Soc. Am.* **96,** 2118–2130, doi 10.1785/0120060036.

Nishenko, S. P., and S. K. Singh (1987). Conditional probabilities for the recurrence of large and Great interplate earthquakes along the Mexican subduction zone, *Bull. Seismol. Soc. Am.* **77,** no. 6, 2095–2114.

Olsen, K. B. (1994). Simulation of three-dimensional wave propagation in the Salt Lake Basin, *Ph.D. Thesis*, University of Utah, 157 p.

Olsen, K. B., R. J. Archuleta, and J. R. Matarese (1995). Three-dimensional simulation of a magnitude 7.75 earthquake on the San Andreas fault, *Science* **270,** 1628–1632.

Pacheco, J., and N. Kostoglodov (1999). Seismicity in Mexico from 1900 to 1999, http://www.ssn.unam.mx/, last accessed July 2011.

Shapiro, N. M., K. B. Olsen, and S. K. Singh (2000). Wave-guide effects in subduction zones: evidence from three-dimensional modeling, *Geophys. Res. Lett.* **27,** 433–436.

Wells, D. L., and K. J. Coppersmith (1994). New empirical relationships among magnitude, rupture length, rupture width, rupture area, and surface displacement, *Bull. Seismol. Soc. Am.* **84,** no. 4, 974–1002.

Institute of Engineering, UNAM
C.U., 04510, Mexico DF, Mexico
(M.C., N.P.)

Department of Geological Sciences
San Diego State University
San Diego
California 92182-1020
(K.B.O.)

CAOS
Universitat Autònoma de Barcelona
08913, Bellaterra (Barcelona), Spain
(E.C.)

Manuscript received 19 July 2010